arXiv:1605.03570v2 [math.NA] 29 Nov 2016

# A Study on Moving Mesh Finite Element Solution of the Porous Medium Equation

Cuong Ngo* Weizhang Huang†

**Abstract**

An adaptive moving mesh finite element method is studied for the numerical solution of the porous medium equation with and without variable exponents and absorption. The method is based on the moving mesh partial differential equation approach and employs its newly developed implementation. The implementation has several improvements over the traditional one, including its explicit, compact form of the mesh velocities, ease to program, and less likelihood of producing singular meshes. Three types of metric tensor that correspond to uniform and arclength-based and Hessian-based adaptive meshes are considered. The method shows first-order convergence for uniform and arclength-based adaptive meshes, and second-order convergence for Hessian-based adaptive meshes. It is also shown that the method can be used for situations with complex free boundaries, emerging and splitting of free boundaries, and the porous medium equation with variable exponents and absorption. Two-dimensional numerical results are presented.

**Key words:** porous medium equation, adaptive moving mesh method, MMPDE method, finite element method, Hessian-based adaptivity, immersed boundary, free boundary

**AMS subject classifications:** 65M60, 65M50, 35Q35

## 1 Introduction

We consider the numerical solution of the initial-boundary value problem (IBVP) of the porous medium equation (PME) in two dimensions,

$$\begin{cases} u_t = \nabla \cdot (|u|^m \nabla u), & \text{in} \quad \Omega \times (t_0, T] \\ u(\boldsymbol{x}, t_0) = u_0(\boldsymbol{x}), & \text{on} \quad \Omega \\ u(\boldsymbol{x}, t) = 0, & \text{on} \quad \partial\Omega \times (t_0, T] \end{cases} \tag{1}$$

where $\Omega$ is a bounded polygonal domain, $u_0(\boldsymbol{x})$ is a given function, and $m \geq 1$ is a physical parameter. PME is a nontrivial generalization of the heat equation. It is found in many areas of the physical sciences, including gas flow in porous medium, incompressible fluid dynamics, nonlinear heat transfer, and image processing; e.g., see [55] and references therein. In the case of gas flow in porous medium, $u$ represents the density of the gas, $u^m$ the pressure, $u\nabla(u^m)$ the flux, $\nabla(u^m)$ the velocity, and $m$ is the isentropic coefficient. In the case of radiation diffusion in plasmas, $m$ stands for the power of temperature appearing in the nonlinear diffusion coefficient and can take

*Department of Mathematics, University of Kansas, Lawrence, KS 66045, U.S.A. (cngo@ku.edu).
†Department of Mathematics, University of Kansas, Lawrence, KS 66045, U.S.A. (whuang@ku.edu).

values up to 5.5 [55, Page 23]. PME itself represents a nonlinear diffusion process. One of its many interesting features is its degeneracy which induces a property of the finite propagation: if $u_0(\boldsymbol{x})$ has a compact support, the solution will have a compact support for any time $t > t_0$. This in effect creates a free boundary that stays between the regions where $u$ is nonzero and where $u$ vanishes and propagates at a finite speed for all time. Contrary to the heat equation which smooths out its initial solutions, PME solution can become nonsmooth even in cases where it has a smooth initial solution. Moreover, for a certain type of initial solutions, the solution can exhibit a waiting-time phenomenon for which the free boundary will not move until a finite amount of time has elapsed. PME has been studied extensively in theory and there is a vast literature, including the earlier work by Oleĭnik et al. [47], Kalašnikov [34], Aronson [2], the more recent work by Shmarev [52, 53], and the monograph by Vázquez [55] and references therein.

The numerical solution of PME has also received considerable attention from researchers. Particularly, error estimates have been obtained for various finite element approximations. For example, using a regularization approach (to avoid degenerate or negative diffusion, for instance, with the diffusion coefficient $|u|^m$ being replaced by $\max(|u|, \epsilon/2)^m$ for some regularization parameter $\epsilon > 0$) and taking $\epsilon = \mathcal{O}(h^{\frac{2m+4}{m^2+4m+2}})$, Rose [49] shows that the error for a P1 finite element (for space) – backward Euler (for time) approximation of PME is bounded by

$$\left(\sum_n \Delta t \|u_h^n - u\|_{L^{m+2}(\Omega)}^{m+2}\right)^{\frac{1}{m+2}} \leq C\left(\Delta t^{\frac{1}{m+1}} + \left(\ln\left(\frac{1}{h}\right)\right)^{\frac{1}{(m+1)(m+2)}} h^{\frac{2}{m+1}}\right), \tag{2}$$

where $h$ is the maximum element diameter and $u_h^n$ is the numerical approximation of $u$ at $t = t_n$. Nochetto and Verdi [45] consider a class of degenerate PDEs which includes PME as a special example and improve the result of [49]. They show that the error for a P1 finite element – 1st-order semi-implicit approximation of PME is bounded by

$$\begin{aligned} &\|u_h - u\|_{L^\infty(0,T;H^{-1}(\Omega))} + \|(u_h)^{m+1} - u^{m+1}\|_{L^2(0,T;L^2(\Omega))} + \left\|\int_0^t ((u_h)^{m+1} - u^{m+1})\right\|_{L^\infty(0,T;H^1(\Omega))} \\ &\quad \leq C\left(\frac{h^2}{\epsilon} + \frac{h^4}{\epsilon^2 \Delta t} + \Delta t\right)^{\frac{1}{2}} \\ &\quad = \mathcal{O}(h^{\frac{m+2}{2(m+1)}}), \quad \text{if} \quad \Delta t = \mathcal{O}(h^{\frac{m+2}{m+1}}), \quad \epsilon = \mathcal{O}(h^{\frac{m}{m+1}}). \end{aligned} \tag{3}$$

For the P1 finite element – backward Euler approximation, error bounds in various norm are obtained, for instance,

$$\|u_h - u\|_{L^\infty(0,T;H^{-1}(\Omega))} \leq C\left(\Delta t + \left(\ln\left(\frac{1}{h}\right)\right)^{\frac{2m+3}{2m+2}} h\right) \tag{4}$$

by Rulla and Walkington [51],

$$\|u_h - u\|_{L^2(0,T;L^2(\Omega))} \leq C h^{\frac{m^2+6m+8}{6m^2+14m+8}} \quad \text{when} \quad \Delta t = \mathcal{O}(h^{\frac{5m+4}{2m}}) \tag{5}$$

by Ebmeyer [19], and

$$\|u_h - u\|_{L^{m+2}(0,T;L^{m+2}(\Omega))} \leq C\left(\Delta t^{\frac{1}{2}} + h + h^{\frac{1}{m+1}\left(\frac{dm}{2m+4}+1\right)}\right)^{\frac{1}{m+2}} \tag{6}$$

by Wei and Lefton [56], where $d$ is the space dimension. It is remarked that these estimates are obtained for quasi-uniform meshes. The convergence rate is first order at best and decreases with

$m$. Some of these estimates are shown to be optimal in the corresponding norm in lieu of the known regularity of the solution of PME. Moreover, it is worth mentioning that Ebmeyer and Liu [20] obtain error estimates in quasi-norm and Emmrich and Šiška [21] prove that a Galerkin finite element – backward Euler approximation converges to the weak solution of PME using the theory of monotone operators. More recently, Duque et al. [16] establish $L^{1+\max(\gamma/2)}$ error bounds for the approximation of a general order continuous Galerkin in space and a general order discontinuous Galerkin in time for PME with a variable exponent $m = \gamma(\boldsymbol{x})$. Zhang and Wu [58] consider the numerical simulation of the one-dimensional PME on a uniform mesh using a high-order local discontinuous Galerkin finite element method. The method can effectively eliminate unwanted, nonphysical oscillations in the computed solution near the free boundary and lead to a high-order convergence rate within the solution support and away from the free boundary.

The low regularity (steep gradient and corner shape near the moving free boundary) and evolving nature of the solution makes adaptive moving mesh methods an attractive tool to improve accuracy in the numerical solution of PME. A number of works exist in this direction. For example, Budd et al. [10] investigate the numerical simulation of self-similarity solutions of one-dimensional PME using the Moving Mesh PDE (MMPDE) moving mesh method [30, 31] and a specially designed monitor function to preserve the scaling invariance of PME. In a series of papers [4, 5, 7] (also see the review paper [6]), Baines and his co-workers study the numerical solution of PME in one and two dimensions using a moving mesh finite element method that is based upon conserving a local proportion of the total mass that is present in the projected initial data. Numerical results show that their method gives a second-order convergence for $m = 1$ but only a first-order convergence for $m = 3$ when a uniform initial mesh is used [5, 6]. For $m = 3$, the second-order convergence can be recovered in one dimension if an optimal initial mesh is used. Unfortunately, such an optimal mesh is significantly more expensive to compute in two dimensions than in one dimension. Recently, Duque et al. [17, 18] present a moving mesh finite element method based on an MMPDE for PME with variable exponents and with/without absorption. The method shows a first-order convergence when tested for the Barenblatt-Pattle solution of PME.

The objective of this paper is to study an adaptive moving mesh finite element method for the numerical solution of PME. The method is also based on an MMPDE but significantly different from the method of [17, 18]. The MMPDE we use is formulated by minimizing an energy (cf. (18)) based on the equidistribution and alignment conditions and the mesh adaptation is controlled through a matrix-valued function (i.e., a metric tensor) instead of a scalar function. The advantage of using a metric tensor is that it provides information not only to control the size of mesh elements but also their shape and orientation. Generally speaking, a so generated mesh has better alignment with the geometry of the physical solution than that with a scalar mesh adaptation function. Moreover, a newly developed compact formulation of the method (cf. (20) and (21)) makes its implementation much easier and more efficient. Mesh adaptation based on the gradient and Hessian of the solution will be considered. The arclength metric tensor (a gradient-based metric tensor) has been widely used in the context of moving mesh methods because it results in more stable mesh movement than a Hessian-based metric tensor and works well for many problems. On the other hand, there is no theoretical guarantee that the arclength metric tensor will lead to the optimal convergence order for piecewise linear interpolation or finite element approximation since the error is determined by the Hessian of the solution in these situations. As a matter of fact, there are problems, although not very common, for which we have to use a Hessian-based metric tensor in order to achieve the optimal convergence order for piecewise linear interpolation or finite element approximation. Interestingly, PME is one of those problems. We shall show that the linear finite element approximation of the Barenblatt-Pattle solution of PME shows a first-order convergence for arclength-based adaptive meshes and a second-order convergence for Hessian-based adaptive meshes.

Another feature of the method that is different from those of Duque et al. [17, 18] and Baines et al. [4, 5, 6, 7] is that PME is solved on a large domain that contains the free boundary for the whole time period under consideration. In this way, there is no need to explicitly trace the movement of the free boundary and thus the method can readily deal with more complicated structures in the solution and in the differential equation. Numerical examples with simple free boundary (such as the Barenblatt-Pattle solution) and more complex and even merging free boundaries will be presented as well as those for PME with variable exponents and absorption.

In addition to the above mentioned MMPDE method, a number of other moving mesh methods have been developed in the past; e.g., see Hirt et al. [25] (ALE – Arbitrary Lagrangian-Eulerian) Miller and Miller [43] (MFE – moving finite element), Liao and Anderson [40] (deformation map), Li et al. [38] (mesh rezoning), Cao et al. [14] (geometric conservation law), Baines et al. [5] (conservation of fraction mass), and Budd and Williams [12] (parabolic Monge-Ampère equation). The interested reader is also referred to the books/review articles [3, 6, 9, 11, 31, 54] and references therein.

The outline of the paper is as follows. Some properties of PME that are relevant to the numerical simulation are described in Section 2. Section 3 is devoted to the description of the moving mesh finite element method, including the linear finite element discretion of PME on a moving mesh and the generation of an adaptive moving mesh using the MMPDE approach. Numerical examples are presented in Sections 4 and 5 for PME and PME with variable exponents and absorption, respectively. Finally, Section 6 contains the conclusions and further comments.

## 2 Properties of the porous medium equation

Before we describe the finite element approximation of IBVP (1), it is instructive to recall some of its properties that are relevant to numerical simulation. First of all, it is known (e.g., see Vázquez [55]) that when $u_0^{m+2} \in L^1(\Omega)$, IBVP (1) has a weak solution $u$ satisfying $u(\cdot,t)^{m+2} \in L^1(\Omega)$ for any $t \in (t_0, T]$ and $u^{m+1} \in L^2(0,T; H_0^1(\Omega))$. Moreover, a nonnegative weak solution exists if $u_0^{m+2} \in L^1(\Omega)$, $u_0 \in L^1(\Omega)$, and $u_0 \geq 0$. The uniqueness of the weak solution is guaranteed if it is further assumed that $u \in L^2(\Omega \times (0,T))$.

PME is degenerate whenever $u = 0$. Due to this degeneracy, PDE has the property of the finite speed of propagation: if compact-supported initially, its solution remains compact-supported at any finite time, with the support monotonically expanding as time evolves. The boundary of the support forms a moving interface $\Gamma(t)$ which is commonly referred to as a free boundary. The velocity of the free boundary is given by Darcy's law (e.g., see Shmarev [52]), i.e.,

$$\Gamma'(t) = -\lim_{\boldsymbol{x} \to \Gamma(t)^-} \nabla \left( \frac{u^m(\boldsymbol{x},t)}{m} \right), \tag{7}$$

where the limit is taken from the interior of the support. In addition, PME exhibits a waiting-time phenomenon: for a certain type of initial solutions the free boundary does not move until a finite amount of time has elapsed. Loosely speaking, from (7) we may expect to see this phenomenon for initial solutions having vanishing $\nabla(u^m)$ at the initial free boundary.

A few classes of special solutions to IBVP (1) have been known, among which is the Barenblatt-Pattle solution, viz.,

$$u(r,t) = \begin{cases} \frac{1}{\lambda^d(t)} \left( 1 - \left( \frac{r}{r_0 \lambda(t)} \right)^2 \right)^{\frac{1}{m}}, & \text{for} \quad |r| \leq r_0 \lambda(t) \\ 0, & \text{for} \quad |r| > r_0 \lambda(t) \end{cases} \tag{8}$$

where

$$r = |\boldsymbol{x}|, \quad \lambda(t) = \left(\frac{t}{t_0}\right)^{\frac{1}{2+dm}}, \quad t_0 = \frac{r_0^2 m}{2(2+dm)},$$

and $r_0 > 0$ is a given parameter. It is radially symmetric, self-similar, and compact-supported for any finite time. Moreover, $u^m$ is Lipschitz continuous in $\boldsymbol{x}$ and $t$ and $\nabla(u^m)$ is bounded in the support of $u(\cdot, t)$, $\text{supp}(u(\cdot, t))$. Furthermore, the solution is Hölder continuous. The slope of the solution at the free boundary is finite for $m = 1$ and becomes infinite when $m > 1$, which causes challenges for the numerical solution of PME. These regularity properties also hold for general compactly supported solutions of (1), and their free boundaries can be shown to be at least Lipschitz continuous in both space and time; e.g., see [2, 13, 15, 52].

# 3 The moving mesh finite element method

In this section we describe the adaptive moving mesh finite element approximation of IBVP (1). To begin with, we note that there are roughly two approaches for solving the IBVP. The first, as used in [49, 58], is to solve PME in a large domain containing the free boundary for the whole time period of the simulation. With this approach, there is no need to explicitly treat the free boundary, which makes the approach more amenable to problems with complex solution supports. The main disadvantage of this approach is that the solution has a corner shape between the regions of zero and nonzero solution values and thus its regularity on the whole domain is at most $H^1$. An $H^1$ regularity often means at best a first-order convergence in the numerical solution as the mesh is refined.

The second approach is to solve the problem only in the region of compact support; e.g., see [5, 17, 18]. One of the advantages of this approach is that a smaller spatial domain is used and thus fewer mesh points can be used to achieve the same computational accuracy. Moreover, the regularity of the solution is better on the support than on a larger domain since it does not have a corner shape. As a result, the numerical solution can have a higher convergence order than that with the first approach. The main disadvantage is that the boundary movement has to be treated explicitly using Darcy's law (7).

We use the first approach in this work. We choose this approach due to its advantage of no need to explicitly treat the free boundary and its potential to deal with problems having complex solution supports. To better resolve the corner shape in the solution and improve the computational accuracy, we employ an MMPDE-based moving mesh method [31] to adaptively and dynamically concentrate the mesh points around the free boundary. Linear finite elements and the fifth-order Radau IIA method (e.g., see Hairer and Wanner [24]) are used for the spatial and temporal discretization, respectively. As we will see in Section 4, a second-order convergence of the finite element approximation in space can be achieved when a properly adapted mesh is used.

## 3.1 Finite element discretization

We now describe the finite element discretization. Denote the time instants by

$$t_0 = 0 < t_1 < \ldots < t_{n_f} \equiv T. \tag{9}$$

For the moment, we assume that the simplicial meshes $\mathcal{T}_h^n$, $n = 0, \ldots, n_f$ for the physical domain $\Omega$ at these time instants are known and have the same connectivity and the same numbers of vertices and elements. (Their generation will be discussed in the next subsection.) Denote the coordinates

of the vertices of $\mathcal{T}_h^n$ by $\boldsymbol{x}_j^n$, $j = 1, ..., N_v$, where $N_v$ is the number of all vertices. The mesh $\mathcal{T}_h(t)$ between any two time instants $t_n$ and $t_{n+1}$ is defined through linear interpolation, i.e.,

$$\boldsymbol{x}_j(t) = \frac{t - t_n}{t_{n+1} - t_n}\boldsymbol{x}_j^{n+1} + \frac{t_{n+1} - t}{t_{n+1} - t_n}\boldsymbol{x}_j^n, \quad \forall j = 1, ..., N_v \tag{10}$$

$$\dot{\boldsymbol{x}}_j(t) = \frac{\boldsymbol{x}_j^{n+1} - \boldsymbol{x}_j^n}{t_{n+1} - t_n}, \quad j = 1, ..., N_v. \tag{11}$$

Denote by $\phi_j(\boldsymbol{x}, t)$ the linear basis function associated with vertex $\boldsymbol{x}_j(t)$. For convenience, we assume that the vertices are arranged such that the first $N_{vi}$ vertices are the interior vertices. Let

$$V_h(t) = \text{span}\{\phi_1(\cdot, t), ..., \phi_{N_{vi}}(\cdot, t)\}.$$

Then, the linear finite element approximation to the solution of IBVP (1) is defined as $u_h(\cdot, t) \in V_h(t)$, $t \in (t_0, T]$ such that

$$\begin{cases} \int_\Omega \frac{\partial u_h}{\partial t} v \; d\boldsymbol{x} = -\int_\Omega |u_h|^m \nabla u_h \cdot \nabla v \; d\boldsymbol{x}, \quad \forall v \in V_h(t), \quad t_0 < t \le T \\ \int_\Omega (u_h(\boldsymbol{x}, 0) - u^0(\boldsymbol{x}))v \; d\boldsymbol{x} = 0, \quad \forall v \in V_h(t). \end{cases} \tag{12}$$

The above equation can be cast in matrix form. Indeed, expressing

$$u_h(\boldsymbol{x}, t) = \sum_{j=1}^{N_{v_i}} u_j(t)\phi_j(\boldsymbol{x}, t)$$

and differentiating it with respect to $t$, we have

$$\frac{\partial u_h}{\partial t} = \sum_{j=1}^{N_{v_i}} \frac{\partial u_j}{\partial t}\phi_j(\boldsymbol{x}, t) + \sum_{j=1}^{N_{v_i}} u_j(t)\frac{\partial \phi_j}{\partial t}.$$

It can be shown (e.g. see Jimack and Wathen [33, Lemma 2.3]) that

$$\frac{\partial \phi_j}{\partial t} = -\nabla \phi_j \cdot \dot{\boldsymbol{X}}, \quad a.e. \text{ in } \Omega$$

where the mesh velocity $\dot{\boldsymbol{X}}$ is defined as

$$\dot{\boldsymbol{X}}(\boldsymbol{x}, t) = \sum_{j=1}^{N_v} \dot{\boldsymbol{x}}_j(t)\phi_j(\boldsymbol{x}, t).$$

Then, we get

$$\frac{\partial u_h}{\partial t} = \sum_{j=1}^{N_{v_i}} \frac{\partial u_j}{\partial t}\phi_j(\boldsymbol{x}, t) - \nabla u_h \cdot \dot{\boldsymbol{X}}.$$

From this and taking $v = \phi_i$ $(i = 1, ..., N_{vi})$ in (12) successively, we obtain

$$\sum_{j=1}^{N_{vi}} \left( \int_\Omega \phi_j \phi_i \; d\boldsymbol{x} \right) \frac{du_j}{dt} = \int_\Omega \nabla u_h \cdot \left( \dot{\boldsymbol{X}}\phi_i - u_h^m \nabla \phi_i \right) \; d\boldsymbol{x}, \quad i = 1, ..., N_{vi}, \quad t_0 < t \le T$$

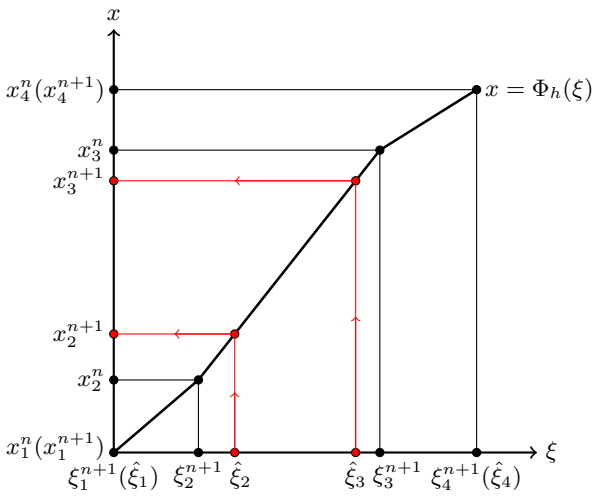


Figure 1: A sketch of the relations among the meshes $\hat{\mathcal{T}}_{c,h} = \{\hat{\boldsymbol{\xi}}_j\}$, $\mathcal{T}_{c,h}^{n+1} = \{\boldsymbol{\xi}_j^{n+1}\}$, $\mathcal{T}_h^n = \{\boldsymbol{x}_j^n\}$, and $\mathcal{T}_h^{n+1} = \{\boldsymbol{x}_j^{n+1}\}$. The function $\boldsymbol{x} = \Phi_h(\boldsymbol{\xi})$ is determined as the correspondence between $\mathcal{T}_{c,h}^{n+1}$ and $\mathcal{T}_h^n$; and $\mathcal{T}_h^{n+1}$ is computed as $\mathcal{T}_h^{n+1} = \Phi_h(\hat{\mathcal{T}}_{c,h})$ using linear interpolation.

which can be cast in the matrix form as

$$B(\boldsymbol{X})\dot{\boldsymbol{U}} = F(\boldsymbol{U}, \boldsymbol{X}, \dot{\boldsymbol{X}}), \tag{13}$$

where $B$ is the mass matrix and $\boldsymbol{X}$ and $\boldsymbol{U}$ are the vectors representing the mesh and solution, respectively. This ODE system is integrated from $t_n$ to $t_{n+1} = t_n + \Delta t_n$ using the fifth-order Radau IIA method, with $\Delta t_n$ being determined by a standard time step size selection procedure (e.g., see Hairer et al. [23, Section II.4]) and using a two-step error estimator of Gonzalez-Pinto et al. [22]. The relative and absolute tolerances $rtol = 10^{-6}$ and $atol = 10^{-8}$ are taken in the computation.

The whole computation alternates between the integration of PME and the generation of the mesh. Starting with the current mesh $\mathcal{T}_h^n$ and a solution $u_h^n(\boldsymbol{x}) \approx u(\boldsymbol{x}, t_n)$ defined thereon, a new mesh $\mathcal{T}_h^{n+1}$ is generated using the moving mesh strategy to be described in the next subsection. Then, the discrete PME (13) is integrated from $t_n$ to $t_{n+1}$ (as described above) to obtain the solution approximation $u_h^{n+1}(\boldsymbol{x})$.

### 3.2 An MMPDE-based moving mesh strategy

We now describe the generation of $\mathcal{T}_h^n$, $n = 1, ..., n_f$. We assume that the mesh $\mathcal{T}_h^n$ and a computed solution $u_h^n(\boldsymbol{x})$ are known at $t = t_n$. We also assume that a reference computational mesh $\hat{\mathcal{T}}_{c,h} = \{\hat{\boldsymbol{\xi}}_j, j = 1, ..., N_v\}$ having the same connectivity and the same numbers of vertices and elements as $\mathcal{T}_h^n$ has been chosen. In our computation, it is taken as a uniform mesh (in the Euclidean metric) defined on $\Omega$. $\hat{\mathcal{T}}_{c,h}$ stays fixed for the whole computation.

The generation of $\mathcal{T}_h^{n+1}$ is through the computational mesh $\mathcal{T}_{c,h} = \{\boldsymbol{\xi}_j, j = 1, ..., N_v\}$ which serves as an intermediate variable. (A sketch of the relations among the meshes $\hat{\mathcal{T}}_{c,h}$, $\mathcal{T}_{c,h}^{n+1}$, $\mathcal{T}_h^n$, and $\mathcal{T}_h^{n+1}$ is shown in Fig. 1.) First, an MMPDE-based mesh equation (to be described below) for the velocities of the computational vertices is employed. It takes the form (cf. (20))

$$\begin{cases} \frac{d\boldsymbol{\xi}_j}{dt} = \boldsymbol{v}_j(\mathbb{M}, \mathcal{T}_h^n; \boldsymbol{\xi}_1, ..., \boldsymbol{\xi}_{N_v}), & j = 1, ..., N_v, \quad t \in (t_n, t_{n+1}] \\ \boldsymbol{\xi}_j(t_n) = \hat{\boldsymbol{\xi}}_j, & j = 1, ..., N_v \end{cases}$$

where $\boldsymbol{v}_j$ denotes the mesh velocity for the $j$-th node which depends on $\mathcal{T}_h^n$, the metric tensor $\mathbb{M}$ defined thereon, and $\mathcal{T}_{c,h}$. Here, the initial mesh is taken to be the reference computational mesh $\hat{\mathcal{T}}_{c,h}$. The system is integrated and the mesh $\mathcal{T}_{c,h}^{n+1} \approx \mathcal{T}_{c,h}(t_{n+1})$ is obtained. During the integration, both $\mathbb{M}$ and $\mathcal{T}_h^n$ are kept fixed. Notice that $\mathcal{T}_{c,h}^{n+1}$ and $\mathcal{T}_h^n$ form a correspondence relation, say, $\boldsymbol{x}_j^n = \Phi_h(\boldsymbol{\xi}_j^{n+1})$, $j = 1, ..., N_v$ or $\boldsymbol{x} = \Phi_h(\boldsymbol{\xi})$. Then, the vertices of the new physical mesh $\mathcal{T}_h^{n+1}$ are defined as $\boldsymbol{x}_j^{n+1} = \Phi_h(\hat{\boldsymbol{\xi}}_j)$, $j = 1, ..., N_v$. Since $\Phi_h$ is defined only at the vertices of $\mathcal{T}_{c,h}^{n+1}$, we need to compute $\Phi_h(\hat{\boldsymbol{\xi}}_j)$ using interpolation. Linear interpolation is used since it is important to keep the nonsingularity of the mesh while it is unnecessary to compute the mesh to high accuracy.

The metric tensor is assumed to be symmetric and uniformly positive definite on $\Omega$. It is used to control the size, shape, and orientation of the elements of the mesh to be generated. We consider three types of mesh, one is uniform and the other two are arclength- and Hessian-based adaptive meshes. The metric tensors associated with the adaptive meshes are defined as

$$\mathbb{M} = (\mathbb{I} + \nabla u_h^n (\nabla u_h^n)^T)^{\frac{1}{2}}, \tag{14}$$

$$\mathbb{M} = \left[\det\left(\mathbb{I} + |H(u_h^n)|\right)\right]^{-\frac{1}{6}} \left(\mathbb{I} + |H(u_h^n)|\right), \tag{15}$$

where $\mathbb{I}$ is the $d \times d$ identity matrix, $H(u_h^n)$ is a recovered Hessian for the piecewise linear finite element solution $u_h^n$, and $|H(u_h^n)| = Q\text{diag}(|\lambda_1|, ..., |\lambda_d|)Q^T$ with $Q\text{diag}(\lambda_1, ..., \lambda_d)Q^T$ being the eigen-decomposition of $H(u_h^n)$. The tensor (14) is the frequently used arclength monitor function which, loosely speaking, places mesh points according to the uniformity in arclength. The tensor (15) is optimal [32] for the $L^2$ norm of linear interpolation error. In our computation, we use a least squares fitting strategy for Hessian recovery (e.g., see [35, 36]).

We now describe the formulation of the MMPDE-based mesh equation. A key component of the formulation is the $\mathbb{M}$-uniform mesh concept with which any (nonuniform) adaptive mesh is viewed as a uniform one in some metric. It is known [27, 31] that such an $\mathbb{M}$-uniform mesh $\mathcal{T}_h$ approximately satisfies the equidistribution and alignment conditions

$$|K|\sqrt{\det(\mathbb{M}_K)} = \frac{\sigma_h |K_c|}{|\Omega_c|}, \quad \forall K \in \mathcal{T}_h \tag{16}$$

$$\frac{1}{d}\text{trace}\left(\left(F_K'\right)^{-1} \mathbb{M}_K^{-1} \left(F_K'\right)^{-T}\right) = \det\left(\left(F_K'\right)^{-1} \mathbb{M}_K^{-1} \left(F_K'\right)^{-T}\right)^{\frac{1}{d}}, \quad \forall K \in \mathcal{T}_h \tag{17}$$

where $|K|$ is the volume of $K$, $\mathbb{M}_K$ is the average of $\mathbb{M}$ over $K$, $\det(\cdot)$ and $\text{trace}(\cdot)$ denote the determinant and trace of a matrix, respectively, $|K_c|$ is the volume of the element $K_c \in \mathcal{T}_{c,h}$ corresponding to $K$, $F_K'$ is the Jacobian matrix of the affine mapping $F_K : K_c \to K$, and

$$\sigma_h = \sum_{K \in \mathcal{T}_h} |K|\sqrt{\det(\mathbb{M}_K)}, \quad |\Omega_c| = \sum_{K_c \in \mathcal{T}_{c,h}} |K_c|.$$

The equidistribution condition (16) requires that the volume of $K$ in the metric $\mathbb{M}$ be proportional to $|K_c|$ with constant proportionality while the alignment condition (17) requires that $K$ be similar to $K_c$. The meshes that closely satisfy these conditions can be obtained by minimizing the energy function

$$\begin{aligned} I_h = \theta \sum_{K \in \mathcal{T}_h} |K|\sqrt{\det(\mathbb{M}_K)} \left(\text{trace}((F_K')^{-1}\mathbb{M}_K^{-1}(F_K')^{-T})\right)^{\frac{dp}{2}} \\ + (1 - 2\theta) d^{\frac{dp}{2}} \sum_{K \in \mathcal{T}_h} |K|\sqrt{\det(\mathbb{M}_K)} \left(\frac{|K_c|}{|K|\sqrt{\det(\mathbb{M}_K)}}\right)^p, \end{aligned} \tag{18}$$

which is a Riemann sum of a continuous functional developed in [26] based on equidistribution and alignment for variational mesh adaptation. Here, $\theta \in (0, \frac{1}{2}]$ and $p > 1$ are non-dimensional parameters. We choose $\theta = 1/3$ and $p = 2$ in our computation.

Notice that $I_h$ is a function of the position of the computational vertices $\{\boldsymbol{\xi}_j\}_{j=1}^{N_v}$ and the physical coordinates $\{\boldsymbol{x}_j\}_{j=1}^{N_v}$. For the current situation, we choose $\mathcal{T}_h$ to be $\mathcal{T}_h^n$ (the current physical mesh). Then, $I_h$ is the function of $\boldsymbol{\xi}_j$, $j = 1, ..., N_v$ only. Instead of taking direct minimization of $I_h$ with respect to these coordinates, we follow the MMPDE approach [30] and define the moving mesh equation as a gradient system of $I_h$,

$$\frac{d\boldsymbol{\xi}_j}{dt} = -\frac{P_j}{\tau}\left[\frac{\partial I_h}{\partial \boldsymbol{\xi}_j}\right]^T, \quad j = 1, ..., N_v \tag{19}$$

where the derivative of $I_h$ with respect to $\boldsymbol{\xi}_j$, $\partial I_h/\partial \boldsymbol{\xi}_j$, is considered as a row vector, $\tau > 0$ is a parameter used to control the response time of the mesh movement to the change in the metric tensor, and $P_j = \det(\mathbb{M}(\boldsymbol{x}_j))^{\frac{p-1}{2}}$ is chosen such that (19) is invariant under the scaling transformation of $\mathbb{M}$: $\mathbb{M} \to c\mathbb{M}$ for any positive constant $c$. The derivative of $I_h$ with respect to $\boldsymbol{\xi}_j$ can be found analytically using the notion of scalar-by-matrix differentiation; see [28]. With these analytical formulas, we can rewrite (19) into

$$\frac{d\boldsymbol{\xi}_j}{dt} = \frac{P_j}{\tau}\sum_{K\in\omega_j} |K|\boldsymbol{v}_{j_K}^K, \quad j = 1, \ldots, N_v \tag{20}$$

where $\omega_j$ is the element patch associated with the $j$-th vertex, $j_K$ is its local index of the vertex on $K$, and $\boldsymbol{v}_{j_K}^K$ is the velocity contributed by the element $K$ to the vertex $j_K$. The velocities contributed by $K$ to its vertices are given by

$$\begin{bmatrix} (\boldsymbol{v}_1^K)^T \\ \vdots \\ (\boldsymbol{v}_d^K)^T \end{bmatrix} = -E_K^{-1}\frac{\partial G}{\partial \mathbb{J}} - \frac{\partial G}{\partial \det(\mathbb{J})}\frac{\det(\hat{E}_K)}{\det(E_K)}\hat{E}_K^{-1}, \quad \boldsymbol{v}_0^K = -\sum_{i=1}^{d}\boldsymbol{v}_d^K, \tag{21}$$

where $E_K = [\boldsymbol{x}_1^K - \boldsymbol{x}_0^K, ..., \boldsymbol{x}_d^K - \boldsymbol{x}_0^K]$ is the edge matrix of $K$, $\hat{E}_K$ is the edge matrix for $K_c$ which is defined similarly, the function $G$ is associated with the energy (18) and defined as

$$G(\mathbb{J}, \det(\mathbb{J}), \mathbb{M}) = \theta\sqrt{\det(\mathbb{M})}\left(\mathrm{trace}(\mathbb{J}\mathbb{M}^{-1}\mathbb{J}^T)\right)^{\frac{dp}{2}} + (1-2\theta)d^{\frac{dp}{2}}\sqrt{\det(\mathbb{M})}\left(\frac{\det(\mathbb{J})}{\sqrt{\det(\mathbb{M})}}\right)^p,$$

and its derivatives (evaluated at $(\mathbb{J}, \det(\mathbb{J}), \mathbb{M}) = ((F_K')^{-1}, \det(F_K')^{-1}, \mathbb{M}_K)$) with respect to the first (the Jacobian matrix) and second arguments are given by

$$\begin{aligned}
\frac{\partial G}{\partial \mathbb{J}} &= dp\theta\sqrt{\det(\mathbb{M})}\left(\mathrm{trace}(\mathbb{J}\mathbb{M}^{-1}\mathbb{J}^T)\right)^{\frac{dp}{2}-1}\mathbb{M}^{-1}\mathbb{J}^T, \\
\frac{\partial G}{\partial \det(\mathbb{J})} &= p(1-2\theta)d^{\frac{dp}{2}}\det(\mathbb{M})^{\frac{1-p}{2}}\det(\mathbb{J})^{p-1}.
\end{aligned}$$

Notice that $\partial G/\partial \mathbb{J}$ is a $d$-by-$d$ matrix.

In practical computation, we can first compute the local velocities $\boldsymbol{v}_j^K$, $j = 0, ..., d$ for all elements using (21) and then obtain the velocity for any mesh point by summing the volume weighted contributions from its neighboring elements (cf. (20)). The mesh equation should be

modified for boundary mesh points. For fixed points (such as corners), we can set the velocity to be zero. For those on a boundary edge or surface, the mesh velocities should be modified such that they do not move out of the domain.

The mesh equation (20) (with proper modifications for boundary mesh points) is integrated from $t = t_n$ to $t_{n+1}$ starting with $\hat{\mathcal{T}}_{c,h}$ as the initial mesh. In our computation, the Matlab ODE solver *ode15s* (an implicit scheme) is used to integrate (20).

Equation (20) is called the $\boldsymbol{\xi}$-formulation of the MMPDE moving mesh method since it has been formulated in terms of the derivatives of $I_h$ with respect to $\boldsymbol{\xi}_j$ and the velocities for the computational coordinates. We can obtain an $\boldsymbol{x}$-formulation by directly differentiating $I_h$ with respect to $\boldsymbol{x}_j$ (with $\mathcal{T}_{c,h}$ being taken as $\hat{\mathcal{T}}_{c,h}$ and fixed) and the new physical mesh $\mathcal{T}_h^{n+1}$ by directly integrating this formulation. The main disadvantage of this formulation is that its formula is more complicated than that of the $\boldsymbol{\xi}$-formulation and the metric tensor, which is defined on $\mathcal{T}_h^n$, needs to be updated every time the physical mesh is changed during the time integration of the mesh equation for $\mathcal{T}_h^{n+1}$. It is analytically shown in [29] that the mesh governed by the $\boldsymbol{x}$-formulation will stay nonsingular when it is nonsingular initially. Although such a theoretical result is not available for the $\boldsymbol{\xi}$-formulation, our limited numerical experience shows that the $\boldsymbol{\xi}$-formulation also produces nonsingular meshes.

# 4 Numerical Results for PME

In this section we present numerical results obtained with the moving mesh finite element method described in the previous section for a number of PME examples. They include the Barenblatt-Pattle solution and the generalizations of several one-dimensional examples studied by Zhang and Wu [58]. These examples are selected to demonstrate the accuracy of our method as well as its ability to deal with solutions having complex support and the waiting-time phenomenon. For the cases having an exact solution, the error in the computed solution will be measured in the (global) $L^2$ norm, i.e.,

$$\|e_h\|_{L^2(t_0,T;L^2(\Omega))} = \left( \int_{t_0}^{T} \int_{\Omega} e_h^2(\boldsymbol{x},t) d\boldsymbol{x} dt \right)^{\frac{1}{2}}.$$

We choose this norm because various error estimates are obtained in this norm, e.g., see (5). (An exception is Fig. 4 where the convergence history in $L^1$ norm is plotted for comparison purpose.) In our computation, we use $\tau = 10^{-4}$ (for the mesh movement), the maximal allowed time step size $\Delta t_{max} = 10^{-3}$ (for integrating PME), and the Hessian-based metric tensor (15), unless stated otherwise.

*Example* 4.1 (Barenblatt-Pattle solution). We first consider the Barenblatt-Pattle solution (8) with $r_0 = 0.5$ and $T = (t_0 + 0.1)/2$. We use it to verify the accuracy of the numerical method and the effects of the mesh adaptivity and the physical parameter $m$ on the computational accuracy.

Typical meshes and computed solutions at the final time obtained with the uniform mesh and two adaptive mesh strategies are shown in Fig. 2 and the convergence history is shown in Fig. 3 for the cases $m = 1$ and 2. We can see that for both uniform and the arclength-based adaptive meshes, the convergence order is about 1.5 (i.e., $\mathcal{O}(N^{-\frac{1.5}{2}})$) for $m = 1$ and 1 for the case $m = 2$, with an arclength-based adaptive mesh producing slightly more accurate solutions for both cases. We notice that the exact solution (8) is in $H^1(\Omega)$ for $m = 1$ and $W^{1,\frac{m}{m-1}-\epsilon}(\Omega)$ for $m > 1$, where $\epsilon$ is a small positive number. The observed convergence order is higher than what we can expect from the solution regularity. (For example, the theoretical estimate (5) shows a convergence order of 15/28 for $m = 1$ and 6/15 for $m = 2$.) Even more surprisingly, Hessian-based adaptive meshes

lead to a second-order convergence rate for both the $m = 1$ and 2 cases. We do not have a rigorous explanation for this but would like to point out two relevant observations. The first is that the mesh is denser near the free boundary with the Hessian-based metric tensor than with the arclength metric tensor (e.g., see Fig. 2). The other is that the exact solution has higher regularity in its support than on the whole domain $\Omega$. Indeed, it can be directly verified that

$$\sqrt{\det(|H(u(\cdot,t))|)} \in L^{\frac{2m}{3m-2}-\epsilon}(\text{supp}(u(\cdot,t))),$$

where $\epsilon$ is a small positive number and $H(u(\cdot,t))$ denotes the Hessian of $u$. It is known [32] that for an $\mathbb{M}$-uniform mesh associated with the metric tensor (15), the linear interpolation error on a polygonal domain $D$ is bounded by

$$\|u - \Pi_1 u\|_{L^2(D)} \le CN^{-1} \|\sqrt{\det(|H(u)|)}\|_{L^{\frac{2}{3}}(D)} + h.o.t.,$$

where *h.o.t.* stands for higher-order terms. From this we can expect a second-order convergence if we consider linear interpolation only in the support of the solution with a Hessian-based adaptive mesh. Although this analysis does not apply directly to our current situation with a larger domain than the support, it may shed some light on why the scheme with Hessian-based adaptive meshes shows a second-order convergence.

For comparison purpose, we plot the convergence history in the $L^1$ norm in Fig. 4. It can be seen that the the $L^1$ norm of the error behaves similarly as the $L^2$ norm.

We have seen from Figs. 3 and 4 that mesh adaptation, especially the Hessan-based one, can significantly improve the accuracy. But this comes with additional cost. To show if the mesh adaptation can also improve the efficiency, we plot the solution error against the required CPU time (in seconds) in Fig. 5 for the computation corresponding to Fig. 3b. We can see that a uniform mesh is more efficient when low accuracy is desired while mesh adaptation shows advantages for high accuracy. This is consistent with our limited experience with adaptive moving mesh computation (also see [31, Page 17]). The location of the break-even point depends on specific problems and specific mesh adaptation strategies. For the current situation, we have $(N, \|e_h\|_{L^2}) \approx (300, 3\times 10^{-4})$ for Hessian-based adaptation and $(5000, 10^{-4})$ for arclength-based adaptation.

We now examine the effects of the parameter $\tau$ on the accuracy. Recall that $\tau$ is used in the moving mesh equation (19) to adjust the response time of the mesh movement to the changes in the metric tensor. The smaller $\tau$ is, the faster the response is. On the other hand, for smaller $\tau$, the mesh equation (20) becomes stiffer and harder to integrate. Fortunately, this only causes a slight increase in the cost when an implicit solver (Matlab solver *ode15s* in our computation) is used for the mesh equation. The convergence history is shown in Fig. 6 for Hessian-based adaptive meshes for $\tau = 10^{-2}, 10^{-3}$, and $10^{-4}$. We can see that for both cases with $m = 1$ and $m = 2$, the convergence with $\tau = 10^{-2}$ and $10^{-3}$ slows down when the mesh is becoming finer whereas that with $\tau = 10^{-4}$ stays second order at least for the same considered range of the number of mesh elements. This indicates that the mesh concentration needs to follow up the movement of the free boundary very closely or otherwise we may lose the accuracy improvements gained with mesh adaptation.

Next, we consider the effects of the physical parameter $m$. As seen in Section 2, the solution at the free boundary becomes steeper for larger $m$. It is not surprising that PME will also become more difficult to solve numerically. Indeed, as we can see in Fig. 7a, the convergence rate for the uniform mesh decreases as $m$ increases. This is qualitatively consistent with the theoretical analysis for various finite element approximations for PME on quasi-uniform meshes which also shows a decrease in convergence order with $m$; cf. (2), (3), (5), and (6) and e.g., see [19, 20, 45, 50]. On the other hand, for Hessian-based adaptive meshes the convergence order is second for $m = 1$,

2, and 3, although the error is larger for larger $m$; see Fig. 7b. The final mesh and computed solution obtained for $m = 3$ with the Hessian-based mesh adaptation are shown in Fig. 8.

It is worth pointing out that there are small oscillations around the free boundary in computed solutions; e.g., see Fig. 9. This is due to the nature of the problem where the solution is steep and has a corner shape near the free boundary and the loss of the maximum principle in the discretization. A standard finite element discretization like the one we used here typically leads to solutions with oscillations for this type of problems (also see Zhang and Wu [58] for the case with the one-dimensional PME). The oscillations may be suppressed using, for instance, monotone schemes (e.g., see [8, 44, 46]) or structure-preserving schemes (e.g., see [41, 42, 48, 57, 58, 59]). These schemes and their combination with adaptive mesh movement for PME are worth future investigations. □

*Example* 4.2 (Solution with complex support). We now consider examples with complex solution support. The first example models the movement and interaction of two columns of a substance, which start out with the same height. It has

$$m = 5, \quad \Omega = (-5.5, 5.5) \times (-5.5, 5.5),$$

$$u_0(x, y) = \begin{cases} 1, & \text{for} \quad (x, y) \in (0.5, 3) \times (0.5, 3) \\ 1, & \text{for} \quad (x, y) \in (-3, -0.5) \times (-3, -0.5) \\ 0, & \text{otherwise.} \end{cases} \tag{22}$$

A typical adaptive mesh and the corresponding computed solution obtained with the Hessian-based mesh adaptation are shown in Fig. 10. It can be seen that as time evolves, the support of the solution expands from the two boxes, and then merges into one big region. The mesh adaptation strategy works nicely for the current example, with the mesh points moving to concentrate around the free boundary. Particularly, the mesh stays concentrated and nonsingular even during the merging process of the two separated support regions. Moreover, the numerical results show that the support of the solution becomes smoother as time evolves, consistent with the theoretical prediction (e.g., see [52]). □

*Example* 4.3 (Solution with complex support). The next example is similar to the previous one except that the initial solution has different heights in the two boxes,

$$u_0(x, y) = \begin{cases} 1, & \text{for} \quad (x, y) \in (0.5, 3) \times (0.5, 3) \\ 1.5, & \text{for} \quad (x, y) \in (-3, -0.5) \times (-3, -0.5) \\ 0, & \text{otherwise.} \end{cases} \tag{23}$$

A typical adaptive mesh and the corresponding solution are shown in Fig. 11. Once again, the mesh is concentrated correctly around the free boundaries as they evolve with time. Moreover, the region with larger initial solution values expands faster than the region with smaller values. Overall, the support of the solution for this example expands faster than that of the previous example. At $t = 50$, the two boxes have already merged into a single region of calabash shape. □

*Example* 4.4 (Waiting-time phenomenon). From Section 2 we recall that PME exhibits the waiting-time phenomenon for a certain type of initial solutions. To see this, we consider

$$m = 8, \quad \Omega = (-\pi, \pi) \times (-\pi, \pi),$$

$$u_0(x, y) = \begin{cases} \cos(\sqrt{x^2 + y^2}), & \text{for} \quad \sqrt{x^2 + y^2} \le \frac{\pi}{2} \\ 0, & \text{otherwise.} \end{cases} \tag{24}$$

We have

$$\nabla \cos^m(\sqrt{x^2+y^2}) = -\frac{m\,\cos^{m-1}(\sqrt{x^2+y^2})\,\sin(\sqrt{x^2+y^2})}{\sqrt{x^2+y^2}} \begin{bmatrix} x \\ y \end{bmatrix},$$

which diminishes at $\sqrt{x^2+y^2} = \frac{\pi}{2}$. From Darcy's law (7), we do not anticipate that the free boundary moves initially.

In Figs. 12 and Fig. 13 we show the cross section at $y = 0$ of a computed solution and the solution itself. The results show that the free boundary of the solution does not move until around $t = 10$. Before this time, the solution is steepening. Interestingly, the steepening does not occur on the whole initial support. Instead, it first occurs on a smaller region inside the support and then this region is expanding until it fills the whole initial support. After that, the free boundary waits until it becomes sufficiently steep and then moves. □

# 5 Numerical experiment for PME with variable exponents and absorption

To demonstrate the robustness of the moving mesh finite element method described in Section 3, we consider its application to PME with absorption and/or variable exponents,

$$u_t = \nabla \cdot (|u|^\gamma \nabla u) - \lambda u^\sigma, \quad \Omega \times (t_0, T] \tag{25}$$

subject to a homogeneous Dirichlet boundary condition and an initial condition. Here, $\gamma = \gamma(\boldsymbol{x}, t)$ and $\sigma = \sigma(\boldsymbol{x}, t)$ are nonnegative bounded functions and $\lambda$ is a constant. PME in the form of (25) arises in continuum mechanics to model the motion of a barotropic gas through a porous medium, where the pressure is considered to depend on the density and temperature [1]. Like the standard PME, (25) with constant exponents (i.e., PME with absorption) has been studied extensively; e.g., see [37, 52]. However, there are very few theoretical results for the case with variable exponents [1, 39]. For example, there is no theoretical result on the movement of the free boundary (cf. (7)) although the solution to (25) is known to have the property of finite speed of propagation. Neither is there much numerical work on this situation; see [16, 17, 18].

*Example* 5.1 (Constant exponents with absorption). We first consider an example with an absorption term,

$$\lambda = 1, \quad \gamma = 2, \quad \sigma = 0.1, \quad \Omega = (-1.5\pi, 1.5\pi) \times (-1.5\pi, 1.5\pi),$$
$$u_0 = \begin{cases} |\sin(\sqrt{x^2+y^2})|, & \text{for} \quad \sqrt{x^2+y^2} \in (\frac{\pi}{6}, \pi) \\ 0.5, & \text{for} \quad \sqrt{x^2+y^2} \in [0, \frac{\pi}{6}) \\ 0, & \text{otherwise.} \end{cases}$$

This example is the two-dimensional generalization of a one-dimensional example in [58] that shows a splitting phenomenon in the middle after a finite time.

An adaptive mesh and the corresponding computed solution are shown in Fig. 14. We can see that as time evolves, the solution is becoming lower and the support is expanding on the outer boundary. Meanwhile, the solution is being "punched through" with a hole at the middle of the support. This is an additional feature with the absorption term. □

*Example* 5.2 (Variable exponent without absorption). For this example,

$$\lambda = 0, \quad \gamma = \left(\frac{x}{2}\right)^2 + \left(\frac{y}{2}\right)^2 + 1.1, \quad \Omega = (-2, 2) \times (-2, 2),$$

$$u_0 = \begin{cases} -\sin(2\pi\sqrt{x^2+y^2}), & \text{for} \quad 0.5 < \sqrt{x^2+y^2} < 1 \\ 0, & \text{otherwise.} \end{cases}$$

This example has been studied in [16, 18]. The support of the solution has a hole in the middle which disappears in a finite time. We take $t \in [0, 0.2]$ in the computation. An adaptive mesh and the corresponding numerical solution is shown in Fig. 15. The result appears to have better resolution than that in [16] where a uniform mesh has been used. Moreover, our method works just fine through the closing of the inside hole (cf. Fig. 15) whereas the method in [18] which explicitly traces the free boundary encounters the mesh singularity problem near the time when the hole is closing. □

*Example* 5.3 (Waiting-time for variable exponent without absorption). For this example,

$$\lambda = 0, \quad \gamma = 2 - x - y, \quad \Omega = (-1.5, 1.5) \times (-1.5, 1.5),$$
$$u_0 = \begin{cases} 5(0.25 - x^2 - y^2), & \text{for} \quad \sqrt{x^2+y^2} < 0.5 \\ 0, & \text{otherwise.} \end{cases}$$

This example has been studied in [18]. We take $t \in [0, 0.05]$. The free boundary of the solution does not move until $t \approx 0.02$. A moving mesh and the corresponding computed solution are shown in Fig. 16. We can see that the variation of the exponent causes the free boundary to expand anisotropically and the solution to have different steepness along the free boundary. Moreover, a closer examination of the results confirms the waiting time phenomenon, where the interface in the region $\{(x, y) : x + y \le 0\}$ does not move until a finite time has elapsed. Fig. 17 show the cross sections of the numerical solutions with the plane $y = x$ at various instants of time. In the figure, the red dashed line refers to the position of the initial interface, where the waiting time phenomenon subsequently occurs. □

*Example* 5.4 (Variable exponents with absorption). The last example, taken from [17], has time dependent exponents, i.e.,

$$\lambda = 1, \quad \gamma = \frac{x^2+y^2}{t^2+1}, \quad \sigma = x^2 + y^2 + 1 + e^{-t}, \quad \Omega = (-1.5, 1.5) \times (-1.5, 1.5),$$
$$u_0 = \begin{cases} \cos(2\pi(x^2+y^2)), & \text{for} \quad \sqrt{x^2+y^2} < 0.5 \\ 0, & \text{otherwise.} \end{cases}$$

We take $t \in [0, 0.1]$. The numerical results are shown in Fig. 18. They are comparable with those in [17]. □

## 6 Conclusions and further remarks

In the previous sections we have studied an adaptive moving mesh finite element method for the numerical solution of PME. The method is based on the MMPDE moving mesh strategy and its new implementation and uses a linear finite element method and the fifth-order Radau IIA scheme for the spatial and temporal discretization. Numerical results show that the method is able to produce correct mesh concentration around the free boundary and deal with problems having complex solution support. Three types of mesh have been considered, uniform and acrlength- and Hessian-based adaptive meshes. The method shows a first-order convergence behavior as the mesh is refined for uniform and arclength-based adaptive meshes and improves to a second-order convergence when

Hessian-based adaptive meshes are used. This indicates that mesh concentration around the free boundary is important to the accuracy of the method. Moreover, the prompt response of the mesh movement to the changes in the solution is also crucial, requiring that a small value of the parameter $\tau$ in mesh movement (cf. (19)) be used especially for the computation with fine meshes. We have also studied the application of the method to PME with variable exponents and absorption for which there are very few theoretical results available. Numerical results demonstrate that the method is robust and able to deal with PDEs having more complicated structures.

It should be pointed out that there are small oscillations around the free boundary in computed solutions; see the discussion in Sect. 4. How to suppress these oscillations using a monotone or structure-preserving scheme (e.g., see [8, 41, 42, 44, 46, 48, 57, 58, 59]) and to combine them with adaptive mesh movement for PME are worth future investigations.

**Acknowledgment.** Support from US Army Research Office under grant W911-NF-1510377 is gratefully acknowledged. The authors would also like to thank the anonymous referees for their valuable comments in improving the quality of the paper.

## References

[1] S. N. Antontsev and S. I. Shmarev. A model porous medium equation with variable exponent of nonlinearity: existence, uniqueness and localization properties of solutions. *Nonlinear Anal.*, 60(3):515–545, 2005.

[2] D. G. Aronson. Regularity properties of flows through porous media. *SIAM J. Appl. Math.*, 17:461–467, 1969.

[3] M. J. Baines. *Moving Finite Elements*. Oxford University Press, Oxford, 1994.

[4] M. J. Baines, M. E. Hubbard, and P. K. Jimack. A moving mesh finite element algorithm for fluid flow problems with moving boundaries. *I. J. Numer. Meth. Fluids*, 47:1077–1083, 2005. 8th ICFD Conference on Numerical Methods for Fluid Dynamics. Part 2.

[5] M. J. Baines, M. E. Hubbard, and P. K. Jimack. A moving mesh finite element algorithm for the adaptive solution of time-dependent partial differential equations with moving boundaries. *Appl. Numer. Math.*, 54:450–469, 2005.

[6] M. J. Baines, M. E. Hubbard, and P. K. Jimack. Velocity-based moving mesh methods for nonlinear partial differential equations. *Commun. Comput. Phys.*, 10:509–576, 2011.

[7] M. J. Baines, M. E. Hubbard, P. K. Jimack, and A. C. Jones. Scale-invariant moving finite elements for nonlinear partial differential equations in two dimensions. *Appl. Numer. Math.*, 56:230–252, 2006.

[8] G. Barles and P. E. Souganidis. Convergence of approximation schemes for fully nonlinear second order equations. *Asym. Anal.*, 4:271–283, 1991.

[9] W. Bo and M. Shashkov. R-adaptive reconnection-based arbitrary Lagrangian Eulerian method-R-ReALE. *J. Math. Study*, 48:125–167, 2015.

[10] C. Budd, G. Collins, W. Huang, and R. D. Russell. Self-similar numerical solutions of the porous medium equation using moving mesh methods. *Phil. Trans. R. Soc. Lond. A*, 357:1047–1078, 1999.

[11] C. J. Budd, W. Huang, and R. D. Russell. Adaptivity with moving grids. *Acta Numerica*, 18:111–241, 2009.

[12] C. J. Budd and J. F. Williams. Parabolic Monge-Ampére methods for blow-up problems in several spatial dimensions. *J. Phys. A Math. Gen.*, 39:5425–5444, 2006.

[13] L. A. Caffarelli and A. Friedman. Regularity of the free boundary of a gas flow in an $n$-dimensional porous medium. *Indiana Univ. Math. J.*, 29:361–391, 1980.

[14] W. Cao, W. Huang, and R. D. Russell. A moving mesh method based on the geometric conservation law. *SIAM J. Sci. Comput.*, 24:118–142, 2002.

[15] P. Daskalopoulos and R. Hamilton. Regularity of the free boundary for the porous medium equation. *J. Amer. Math. Soc.*, 11:899–965, 1998.

[16] J. C. M. Duque, R. M. P. Almeida, and S. N. Antontsev. Convergence of the finite element method for the porous media equation with variable exponent. *SIAM J. Numer. Anal.*, 51(6):3483–3504, 2013.

[17] J. C. M. Duque, R. M. P. Almeida, and S. N. Antontsev. Numerical study of the porous medium equation with absorption, variable exponents of nonlinearity and free boundary. *Appl. Math. Comput.*, 235:137–147, 2014.

[18] J. C. M. Duque, R. M. P. Almeida, and S. N. Antontsev. Application of the moving mesh method to the porous medium equation with variable exponent. *Math. Comput. Simulation*, 118:177–185, 2015.

[19] C. Ebmeyer. Error estimates for a class of degenerate parabolic equations. *SIAM J. Numer. Anal.*, 35:1095–1112, 1998.

[20] C. Ebmeyer and W. B. Liu. Finite element approximation of the fast diffusion and the porous medium equations. *SIAM J. Numer. Anal.*, 46:2393–2410, 2008.

[21] E. Emmrich and D. Šiška. Full discretization of the porous medium/fast diffusion equation based on its very weak formulation. *Commun. Math. Sci.*, 10:1055–1080, 2012.

[22] S. González-Pinto, J. I. Montijano, and S. Pérez-Rodríguez. Two-step error estimators for implicit Runge-Kutta methods applied to stiff systems. *ACM Trans. Math. Software*, 30(1):1–18, 2004.

[23] E. Hairer, S. P. Nørsett, and G. Wanner. *Solving Ordinary Differential Equations. I. Nonstiff problems.* Springer-Verlag, Belin, second edition, 1993.

[24] E. Hairer and G. Wanner. *Solving Ordinary Differential Equations. II*, volume 14 of *Springer Series in Computational Mathematics*. Springer-Verlag, Berlin, second edition, 1996. Stiff and differential-algebraic problems.

[25] C. W. Hirt, A. A. Amsden, and J. L. Cook. An arbitrary Lagrangian-Eulerian computing method for all flow speeds. *J. Comput. Phys.*, 14:227–253, 1974.

[26] W. Huang. Variational mesh adaptation: isotropy and equidistribution. *J. Comput. Phys.*, 174:903–924, 2001.

[27] W. Huang. Mathematical principles of anisotropic mesh adaptation. *Comm. Comput. Phys.*, 1:276–310, 2006.

[28] W. Huang and L. Kamenski. A geometric discretization and a simple implementation for variational mesh generation and adaptation. *J. Comput. Phys.*, 301:322–337, 2015. (arXiv:1410.7872).

[29] W. Huang and L. Kamenski. On the mesh nonsingularity of the moving mesh PDE method. submitted, 2015. (arXiv:1512.04971).

[30] W. Huang, Y. Ren, and R. D. Russell. Moving mesh partial differential equations (MMPDEs) based upon the equidistribution principle. *SIAM J. Numer. Anal.*, 31:709–730, 1994.

[31] W. Huang and R. D. Russell. *Adaptive Moving Mesh Methods*. Springer, New York, 2011. Applied Mathematical Sciences Series, Vol. 174.

[32] W. Huang and W. Sun. Variational mesh adaptation II: error estimates and monitor functions. *J. Comput. Phys.*, 184:619–648, 2003.

[33] P. K. Jimack and A. J. Wathen. Temporal derivatives in the finite-element method on continuously deforming grids. *SIAM J. Numer. Anal.*, 28:990–1003, 1991.

[34] A. S. Kalašnikov. Formation of singularities in solutions of the equation of nonstationary filtration. *Ž. Vyčisl. Mat. i Mat. Fiz.*, 7:440–444, 1967.

[35] L. Kamenski. *Anisotropic Mesh Adaptation Based on Hessian Recovery and A Posteriori Error Estimates*. PhD thesis, TU Darmstadt, 2009.

[36] L. Kamenski and W. Huang. How a nonconvergent recovered Hessian works in mesh adaptation. *SIAM J. Numer. Anal.*, 52:1692–1708, 2014. (arXiv:1211.2877).

[37] B. F. Knerr. The behavior of the support of solutions of the equation of nonlinear heat conduction with absorption in one dimension. *Trans. Amer. Math. Soc.*, 249:409–424, 1979.

[38] R. Li, T. Tang, and P. W. Zhang. Moving mesh methods in multiple dimensions based on harmonic maps. *J. Comput. Phys.*, 170:562–588, 2001.

[39] S. Lian, W. Gao, C. Cao, and H. Yuan. Study of the solutions to a model porous medium equation with variable exponent of nonlinearity. *J. Math. Anal. Appl.*, 342:27–38, 2008.

[40] G. J. Liao and D. Anderson. A new approach to grid generation. *Appl. Anal.*, 44:285–298, 1992.

[41] K. Lipnikov, M. Shashkov, D. Svyatskiy, and Y. Vassilevski. Monotone finite volume schemes for diffusion equations on unstructured triangular and shape-regular polygonal meshes. *J. Comput. Phys.*, 227:492–512, 2007.

[42] X. Li and W. Huang. Maximum principle for the finite element solution of time dependent anisotropic diffusion problems. *Numer Meth. P.D.E.*, 29:1963–1985, 2013.

[43] K. Miller and R. Miller. Moving finite elements I. *SIAM J. Numer. Anal.*, 18:1019–1032, 1981.

[44] C. Ngo and W. Huang. Monotone finite difference schemes for anisotropic diffusion problems via nonnegative directional splittings. *Comm. Comput. Phys.*, 19:473–495, 2016.

[45] R. H. Nochetto and C. Verdi. Approximation of degenerate parabolic problems using numerical integration. *SIAM J. Numer. Anal.*, 25:784–814, 1988.

[46] A. M. Oberman. Convergent difference schemes for degenerate elliptic and parabolic equations: Hamilton-Jacobi equations and free boundary problems. *SIAM J. Numer. Anal.*, 44:879–895 (electronic), 2006.

[47] O. A. Oleĭnik, A. S. Kalašinkov, and Y. Čžou. The Cauchy problem and boundary problems for equations of the type of non-stationary filtration. *Izv. Akad. Nauk SSSR. Ser. Mat.*, 22:667–704, 1958.

[48] C. Le Potier. A finite volume method for the approximation of highly anisotropic diffusion operators on unstructured meshes. *Fin. Vol. Complex Appl.*, IV:401-412, 2005.

[49] M. E. Rose. Numerical methods for flows through porous media. I. *Math. Comp.*, 40:435–467, 1983.

[50] M. E. Rose. Numerical methods for flows through porous media. I. *Math. Comp.*, 40:435–467, 1983.

[51] J. Rulla and N. J. Walkington. Optimal rates of convergence for degenerate parabolic problems in two dimensions. *SIAM J. Numer. Anal.*, 33:56–67, 1996.

[52] S. Shmarev. Interfaces in solutions of diffusion-absorption equations in arbitrary space dimension. In *Trends in partial differential equations of mathematical physics*, volume 61 of *Progr. Nonlinear Differential Equations Appl.*, pages 257–273. Birkhäuser, Basel, 2005.

[53] S. I. Shmarev. Interfaces in multidimensional diffusion equations with absorption terms. *Nonlinear Anal.*, 53:791–828, 2003.

[54] T. Tang. Moving mesh methods for computational fluid dynamics flow and transport. In *Recent Advances in Adaptive Computation (Hangzhou, 2004)*, volume 383 of *AMS Contemporary Mathematics*, pages 141–173. Amer. Math. Soc., Providence, RI, 2005.

[55] J. L. Vázquez. *The porous medium equation.* Oxford Mathematical Monographs. The Clarendon Press, Oxford University Press, Oxford, 2007. Mathematical theory.

[56] D. Wei and L. Lefton. A priori $L^\rho$ error estimates for Galerkin approximations to porous medium and fast diffusion equations. *Math. Comp.*, 68:971–989, 1999.

[57] G. Yuan and Z. Sheng. Monotone finite volume schemes for diffusion equations on polygonal meshes. *J. Comput. Phys.*, 227:6288–6312, 2008.

[58] Q. Zhang and Z.-L. Wu. Numerical simulation for porous medium equation by local discontinuous Galerkin finite element method. *J. Sci. Comput.*, 38:127–148, 2009.

[59] Y. Zhang, X. Zhang, and C.-W Shu. Maximum-principle-satisfying second order discontinuous Galerkin schemes for convection-diffusion equations on triangular meshes. *J. Comput. Phys.*, 234:295–316, 2013.

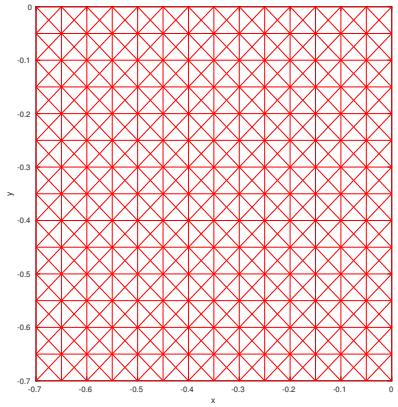

(a) Uniform mesh

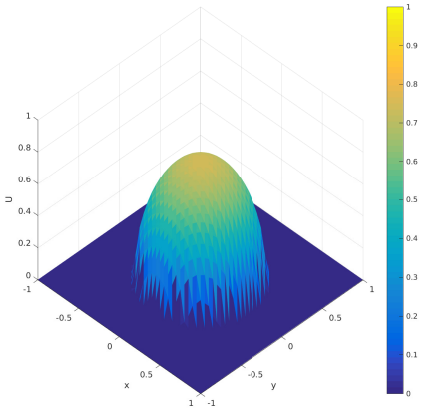

(b) Uniform mesh

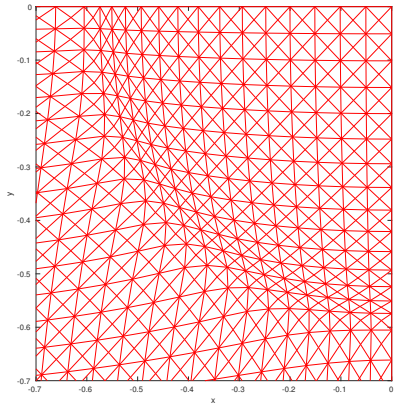

(c) Arclength metric tensor

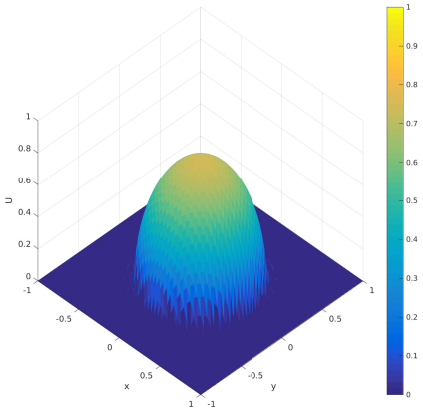

(d) Arclength metric tensor

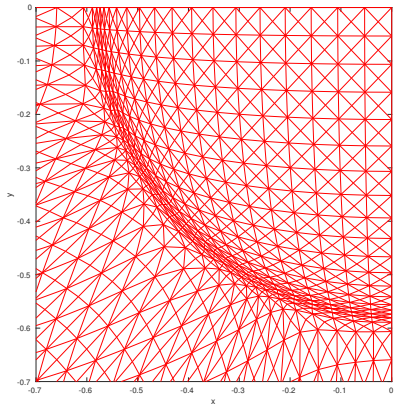

(e) Hessian-based metric tensor

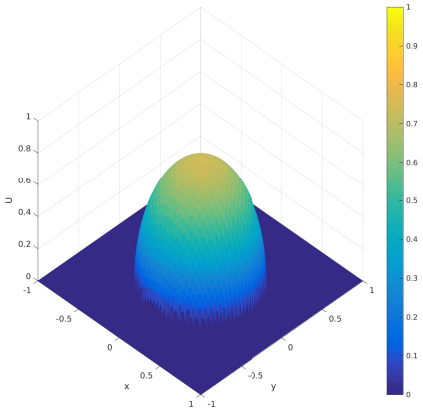

(f) Hessian-based metric tensor

Figure 2: Example 4.1 with $m = 2$. The meshes (closer view near (-0.35, -0.35)) and computed solutions at $t = T$ obtained with uniform and arclength- and Hessian-based adaptive meshes ($N = 25600$).

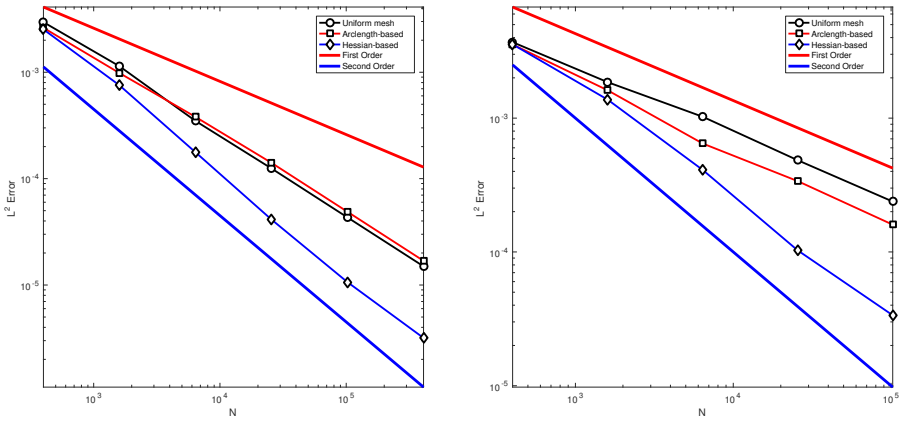


(a) $m = 1$ (b) $m = 2$

Figure 3: Example 4.1. Convergence history (in $L^2$ norm) for the three meshing strategies as $N$ (the number of the elements) increases.

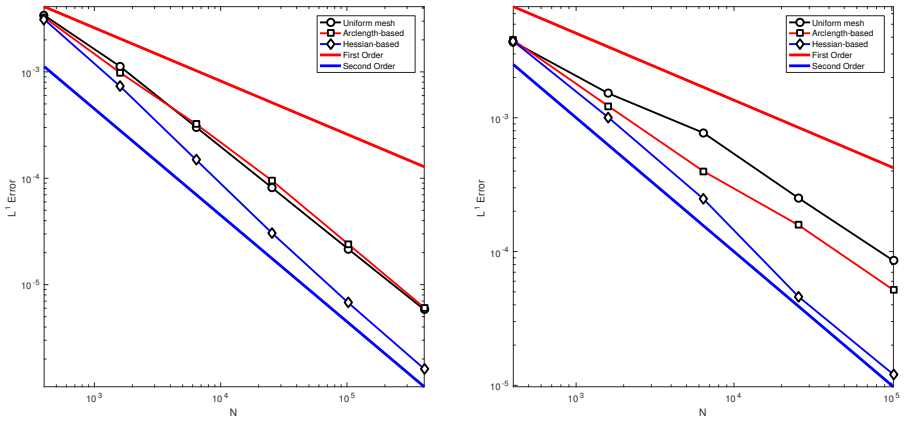


(a) $m = 1$ (b) $m = 2$

Figure 4: Example 4.1. Convergence history (in $L^1$ norm) for the three meshing strategies as $N$ increases.

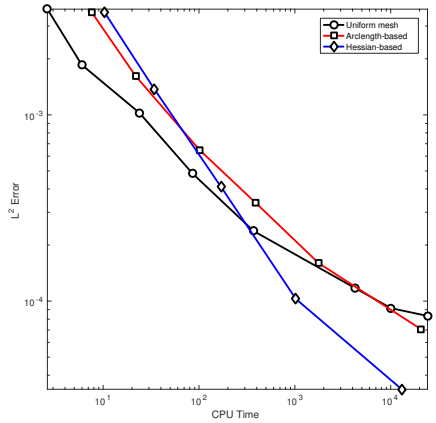


Figure 5: Example 4.1 with $m = 2$. The $L^2$ norm of the error is plotted against the CPU time in seconds for the computation corresponding to Fig. 3b.

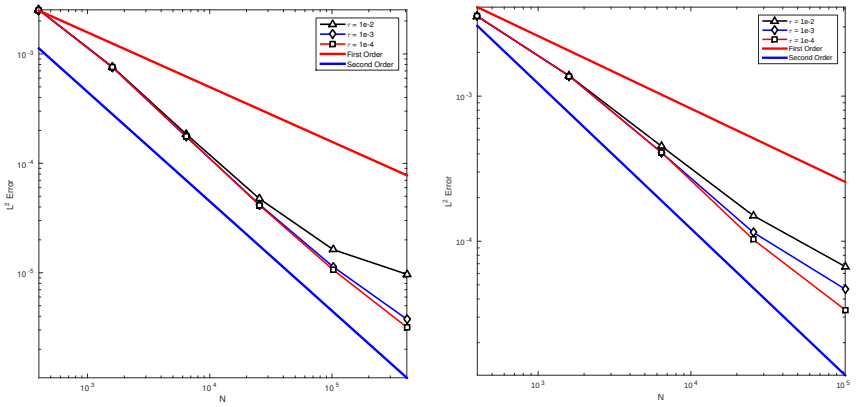


(a) $m = 1$ (b) $m = 2$

Figure 6: Example 4.1. Convergence history for different values of $\tau$.

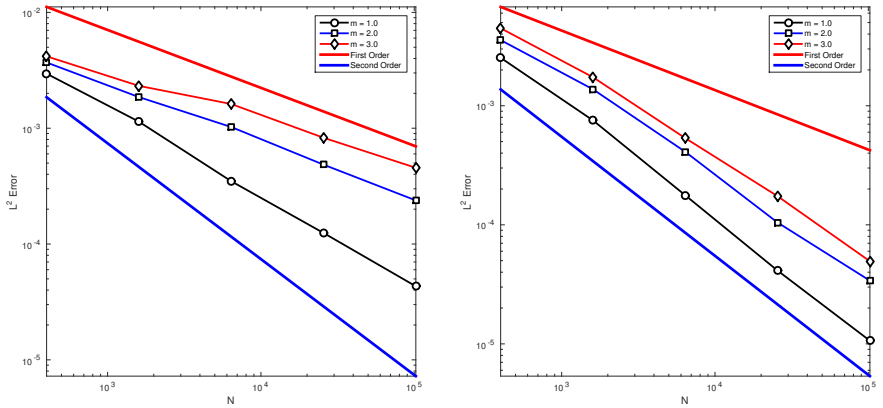


(a) Uniform mesh (b) Hessian-based adaptive mesh

Figure 7: Example 4.1. Convergence history for different values of $m$.

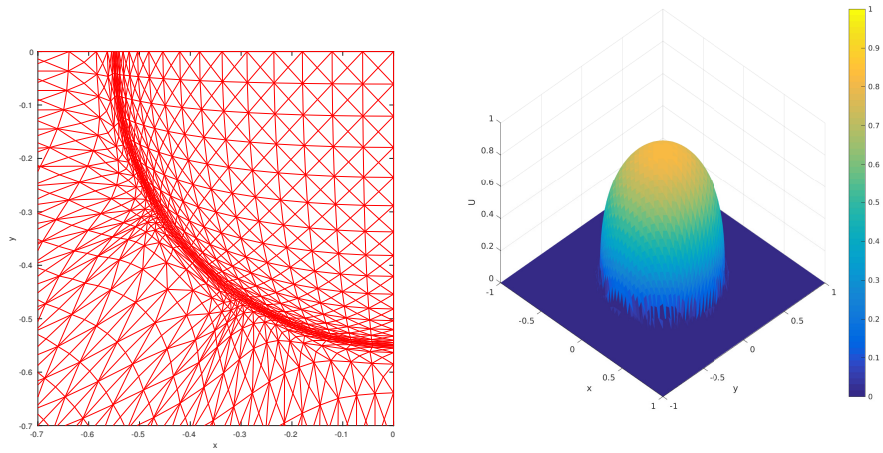

(a) Mesh (b) Computed solution

Figure 8: Example 4.1. The final mesh (close view near (-0.35, -0.35)) and computed solution for $m = 3$ with the Hessian-based mesh adaptation ($N = 25600$).

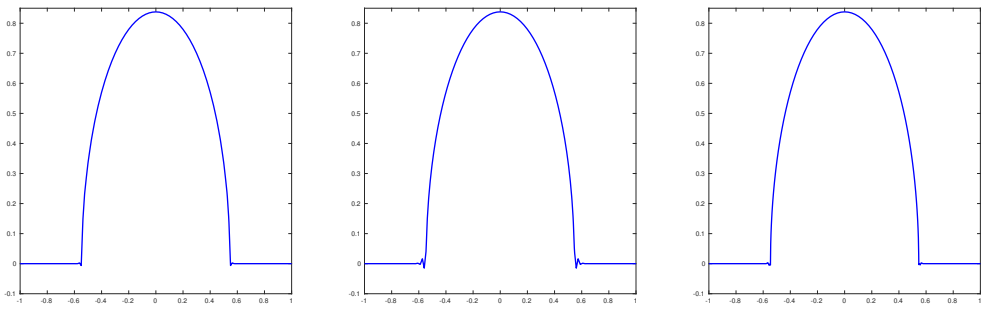

(a) uniform mesh (b) arclength-based mesh (c) Hessian-based mesh

Figure 9: Example 4.1 with $m = 2$. The cross section at $y = 0$ of the computed solutions at $t = T$ obtained with a uniform mesh and arclength- and Hessian-based adaptive meshes ($N = 102,400$).

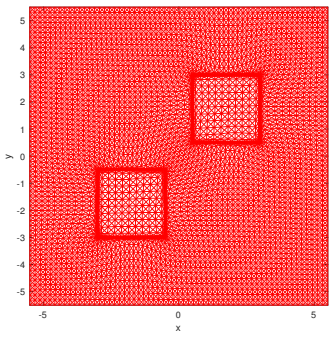

(a) $t = 0$

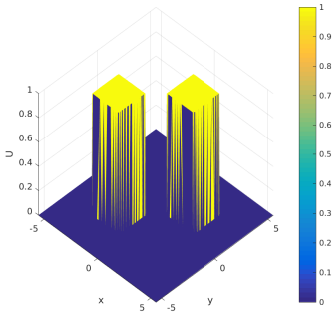

(b) $t = 0$

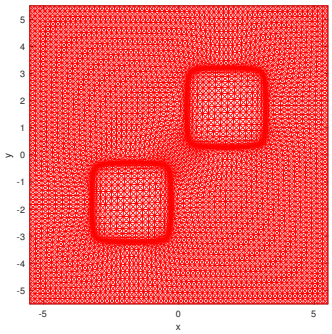

(c) $t = 0.51$

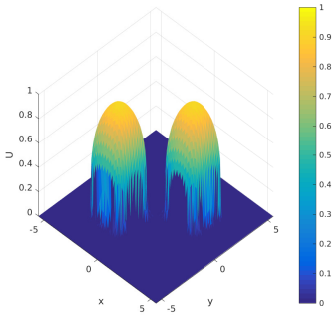

(d) $t = 0.51$

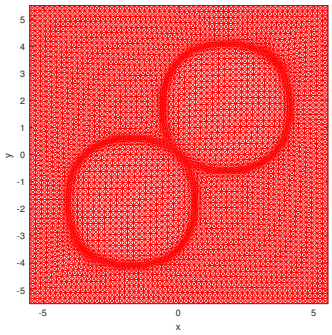

(e) $t = 100.01$

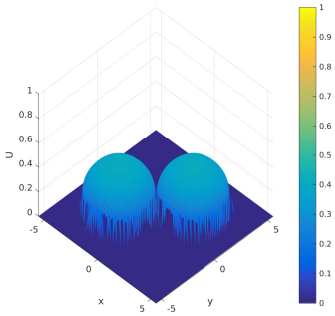

(f) $t = 100.01$

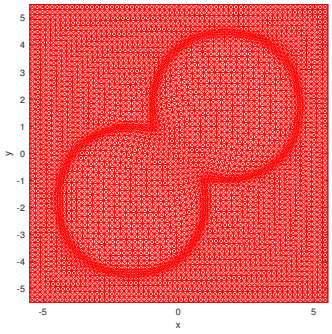

(g) $t = 500$

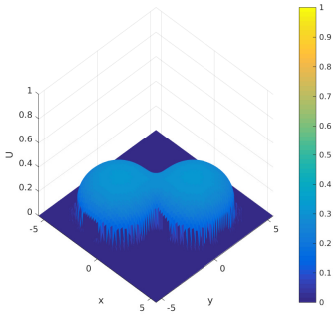

(h) $t = 500$

Figure 10: Example 4.2. An adaptive mesh and the corresponding computed solution at various time instants ($N = 14400$).

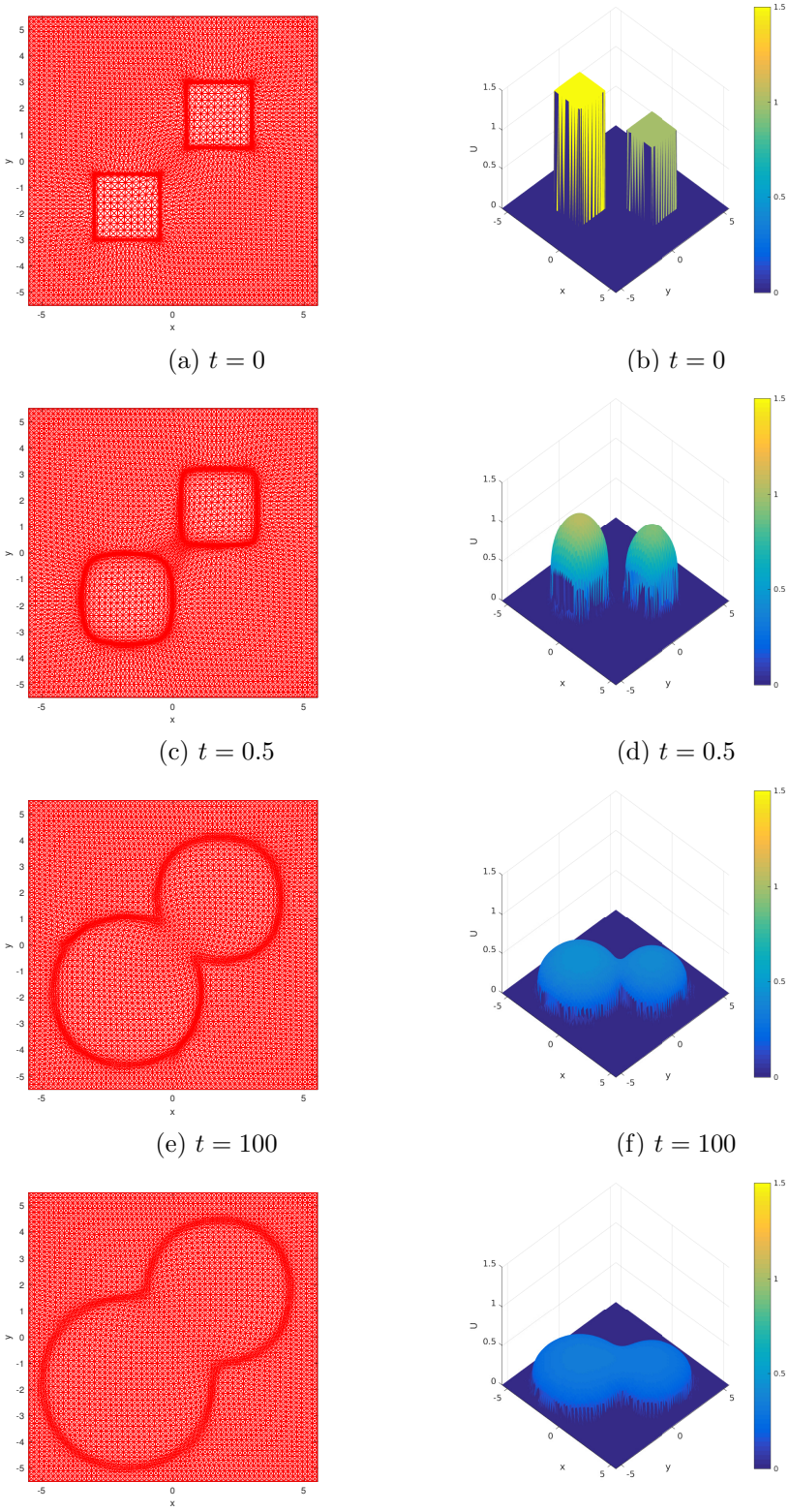

(a) $t = 0$ (b) $t = 0$

(c) $t = 0.5$ (d) $t = 0.5$

(e) $t = 100$ (f) $t = 100$

(g) $t = 500$ (h) $t = 500$

Figure 11: Example 4.3. An adaptive mesh and the corresponding computed solution at various time instants ($N = 14400$).

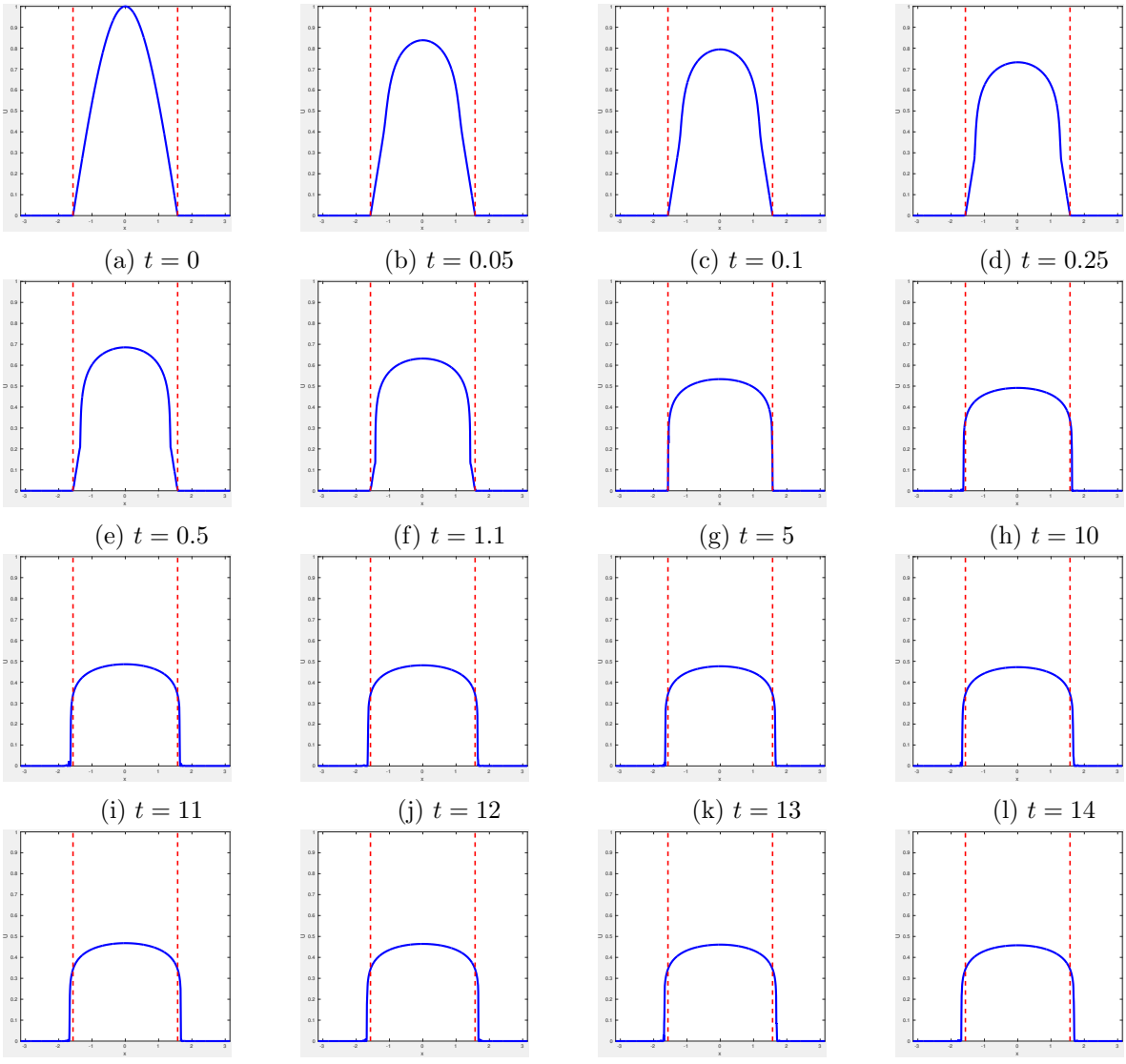

(a) $t = 0$ (b) $t = 0.05$ (c) $t = 0.1$ (d) $t = 0.25$

(e) $t = 0.5$ (f) $t = 1.1$ (g) $t = 5$ (h) $t = 10$

(i) $t = 11$ (j) $t = 12$ (k) $t = 13$ (l) $t = 14$

(m) $t = 15$ (n) $t = 16$ (o) $t = 17$ (p) $t = 18$

Figure 12: Example 4.4. The cross section at $y = 0$ of a computed solution is shown at various time instants ($N = 40000$).

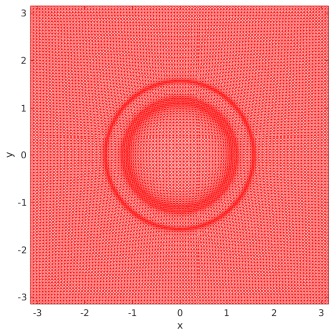

(a) $t = 0.1$

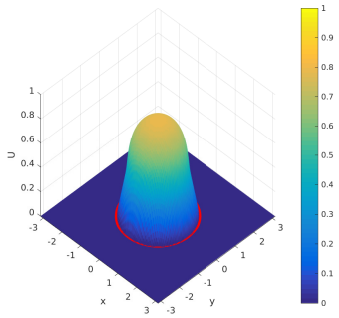

(b) $t = 0.1$

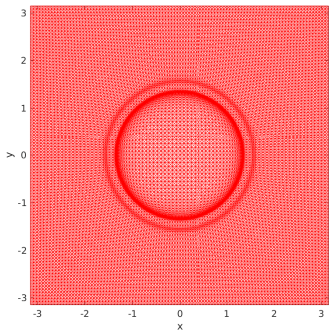

(c) $t = 0.5$

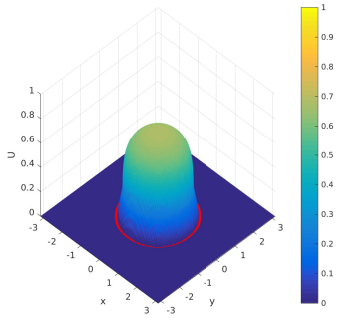

(d) $t = 0.5$

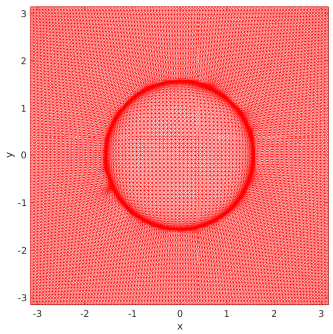

(e) $t = 5$

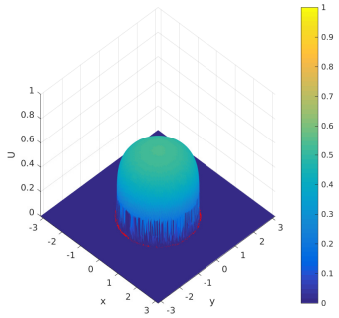

(f) $t = 5$

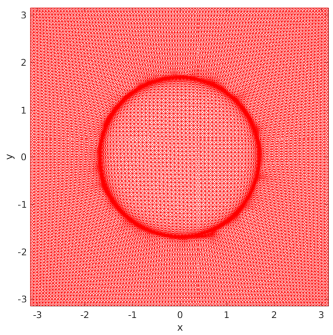

(g) $t = 18.01$

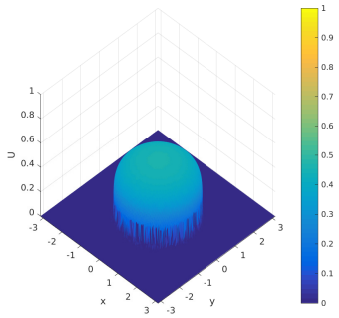

(h) $t = 18.01$

Figure 13: Example 4.4. A computed solution is shown at various time instants ($N = 40000$).

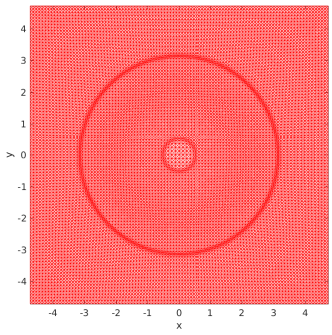

(a) $t = 0$

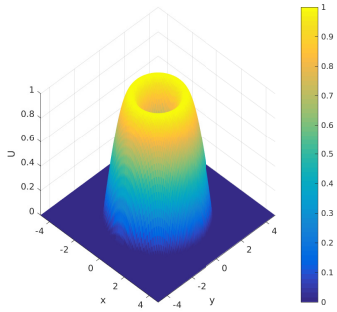

(b) $t = 0$

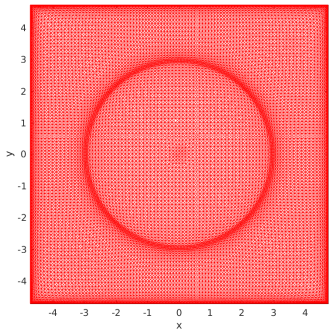

(c) $t = 0.40$

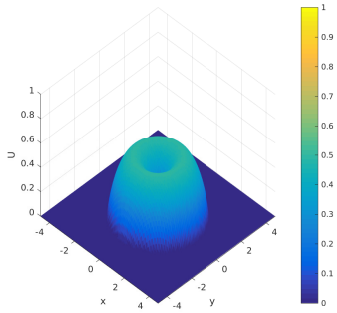

(d) $t = 0.40$

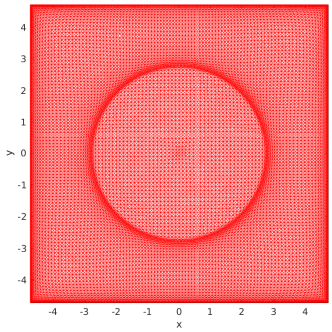

(e) $t = 0.64$

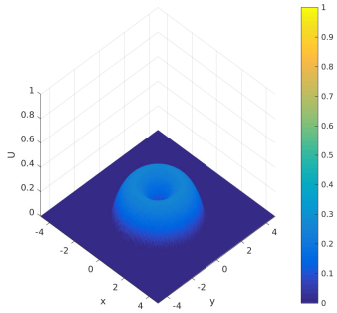

(f) $t = 0.64$

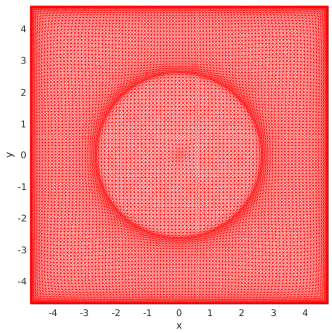

(g) $t = 0.80$

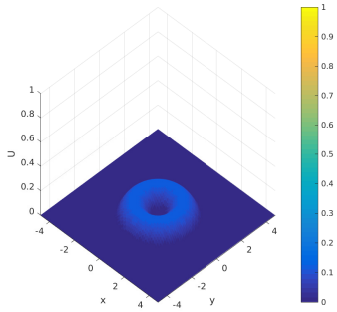

(h) $t = 0.80$

Figure 14: Example 5.1. An adaptive mesh and the corresponding solution at various time instants ($N = 40000$).

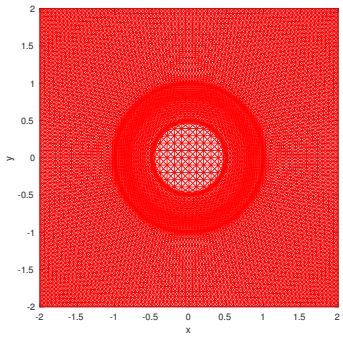

(a) $t = 0$

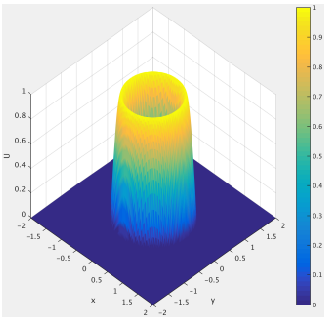

(b) $t = 0$

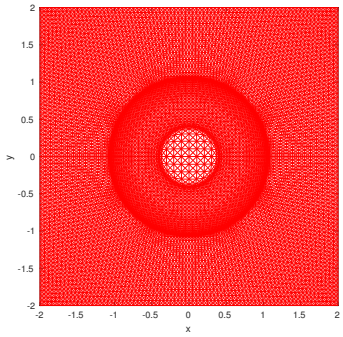

(c) $t = 0.02$

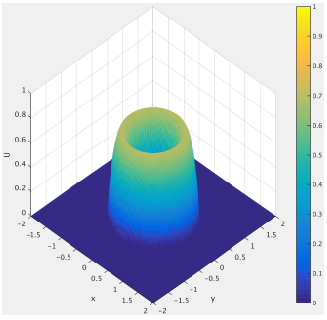

(d) $t = 0.02$

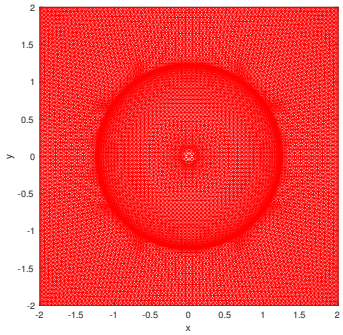

(e) $t = 0.10$

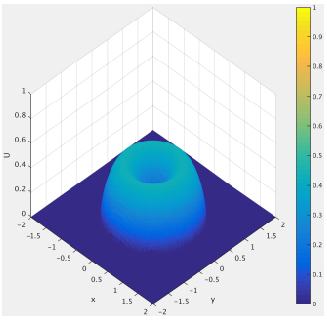

(f) $t = 0.15$

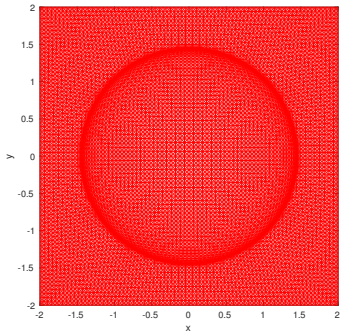

(g) $t = 0.70$

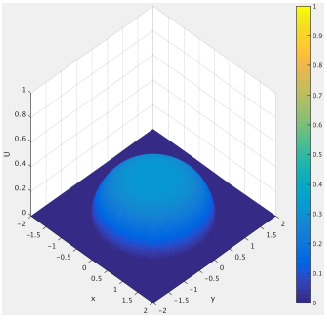

(h) $t = 0.70$

Figure 15: Example 5.2. An adaptive mesh and the corresponding solution at various time instants ($N = 25600$).

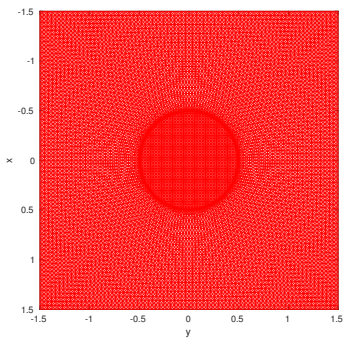

(a) $t = 0$

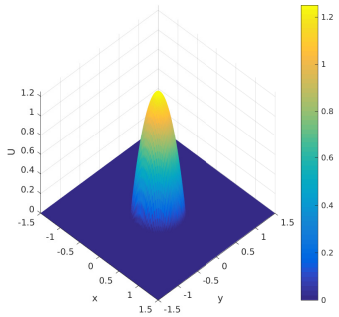

(b) $t = 0$

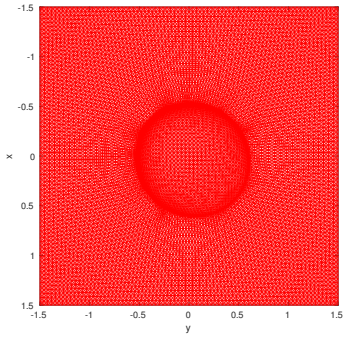

(c) $t = 0.06$

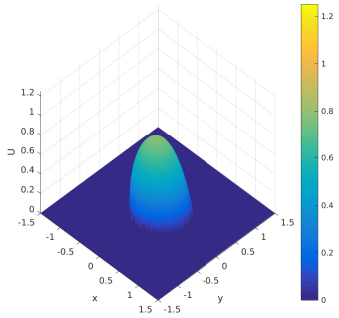

(d) $t = 0.06$

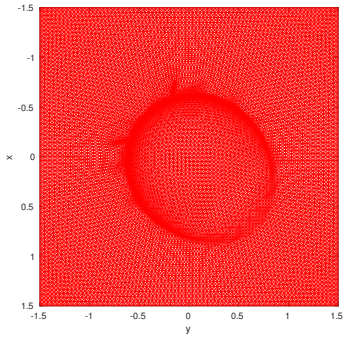

(e) $t = 0.28$

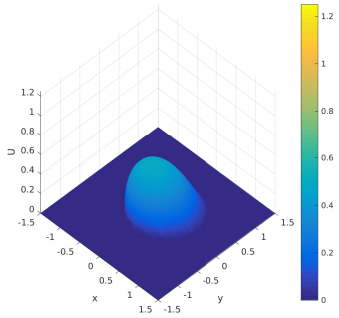

(f) $t = 0.28$

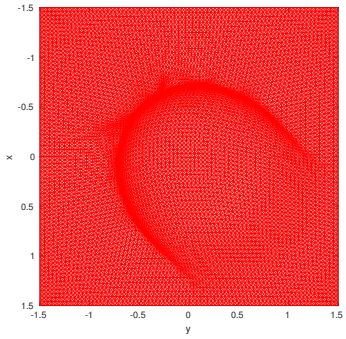

(g) $t = 0.90$

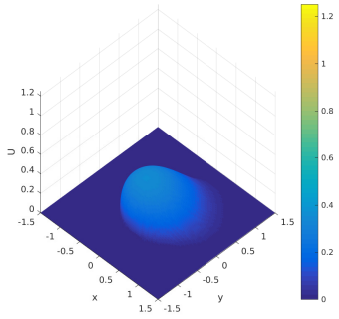

(h) $t = 0.90$

Figure 16: Example 5.3. An adaptive mesh and the corresponding solution at various time instants ($N = 25600$).

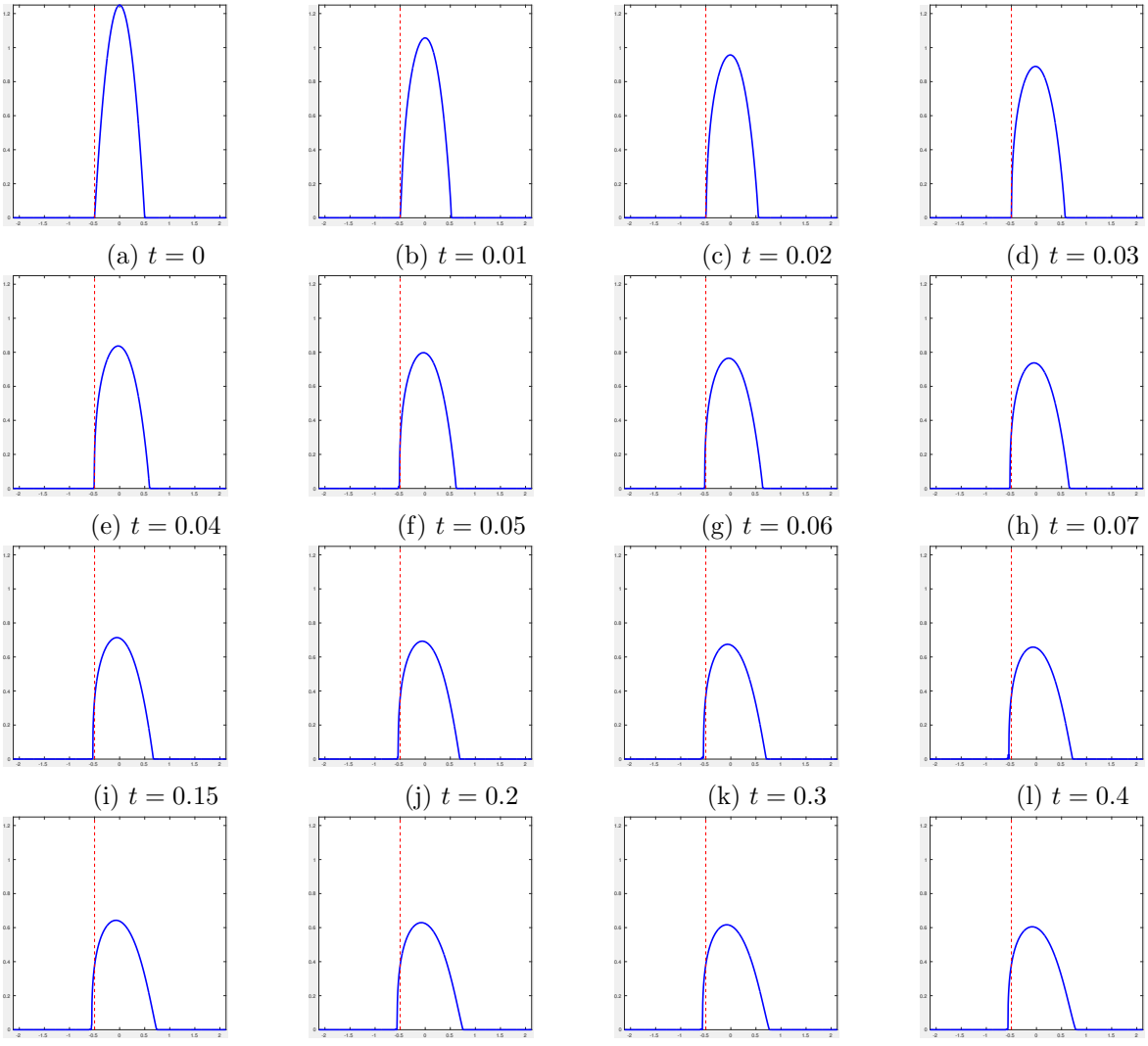

(a) $t = 0$ (b) $t = 0.01$ (c) $t = 0.02$ (d) $t = 0.03$

(e) $t = 0.04$ (f) $t = 0.05$ (g) $t = 0.06$ (h) $t = 0.07$

(i) $t = 0.15$ (j) $t = 0.2$ (k) $t = 0.3$ (l) $t = 0.4$

(m) $t = 0.5$ (n) $t = 0.6$ (o) $t = 0.7$ (p) $t = 0.95$

Figure 17: Example 5.3. The cross section at $y = 0$ of a computed solution is shown at various time instants ($N = 40000$).

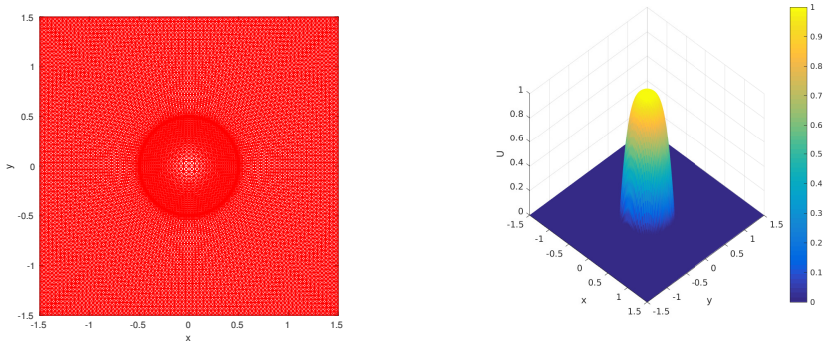

(a) $t = 0.00$ (b) $t = 0$

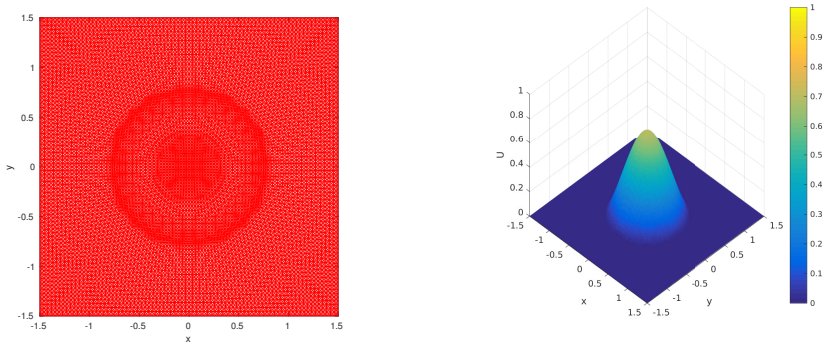

(c) $t = 0.03$ (d) $t = 0.03$

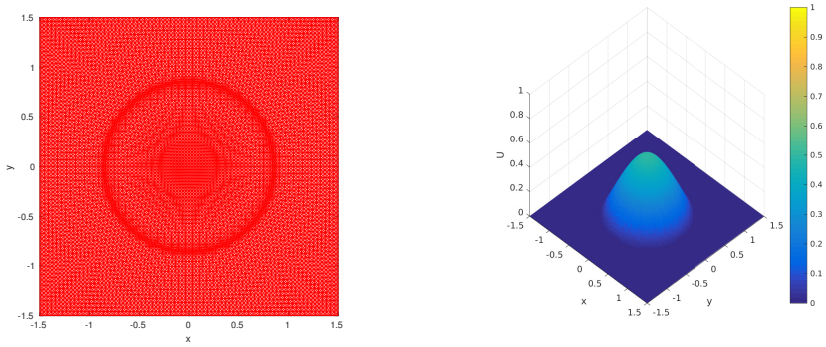

(e) $t = 0.06$ (f) $t = 0.06$

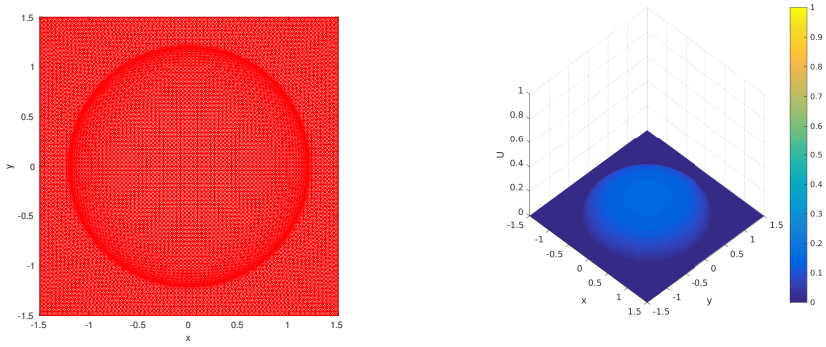

(g) $t = 0.50$ (h) $t = 0.50$

Figure 18: Example 5.4. An adaptive mesh and the corresponding solution at various time instants ($N = 25600$).